UC Berkeley
UC Berkeley Electronic Theses and Dissertations

Title
Biomimetic “Nacre-Like”, Metal-Compliant-Phase Ceramics Produced via Coextrusion

Permalink
https://escholarship.org/uc/item/9tj5b6vd

Author
Wilkerson, Ryan Patrick

Publication Date
2018

Peer reviewed|Thesis/dissertation

eScholarship.org Powered by the California Digital Library
University of California

Biomimetic “Nacre-Like”, Metal-Compliant-Phase Ceramics Produced via Coextrusion

by

Ryan Patrick Wilkerson

A dissertation submitted in partial satisfaction of the
requirements for the degree of
Doctor of Philosophy

in

Engineering - Materials Science and Engineering

in the

GRADUATE DIVISIONS
of the
UNIVERSITY OF CALIFORNIA, BERKELEY

Committee in charge:
Professor Robert Ritchie, Chair
Professor Andrew Minor
Professor Peter Hosemann

Spring 2018

Abstract

Biomimetic “Nacre-Like”, Metal-Compliant-Phase Ceramics Produced via Coextrusion

by

Ryan Patrick Wilkerson
Doctor of Philosophy in Engineering - Materials Science and Engineering

University of California, Berkeley

Professor Robert Ritchie, Chair

Coextrusion is shown to be a viable processing route for the fabrication of bioinspired ceramic materials that exhibit improved damage tolerance. This provides one of the few examples of the synthesis of "nacre-like" ceramic hybrid structures with “brick-and-mortar” architectures using a method that includes a metallic “mortar” (*i.e.*, the compliant phase) during the entire fabrication process, instead of infiltrating it into a pre-fabricated ceramic scaffold. Detailed examination shows how manipulation of such processing can lead to improved mechanical performance in the resulting biomimetic ceramics by obtaining a model high volume fraction (~90 vol. %) ceramic with a brick-and-mortar architecture containing a metallic compliant phase. Specifically, brick-and-mortar alumina hybrid structures were synthesized containing small volume fractions (<10 vol. %) of nickel (Al_2O_3/Ni) which were made by the coextrusion of alumina and nickel oxide in a thermoplastic (polyethylene-ethyl acrylate) suspension. Furthermore the contributions from brick morphology as well as size are examined to extrapolate on the mechanical properties of idealized metal compliant phase brick-and-mortar structures. Flexural strength and crack-initiation fracture toughness values were used to compare the performance of various ceramic architectures, with full crack-growth resistance curves (*R*-curves) measured and compared to similar bioinspired ceramics for the most promising alumina structures. These mechanical tests were performed as a function of temperature to explore the evolution of toughening contributions of the mortar and structure as it relates to changes in the mortar plasticity and to consider the viability of these structures in elevated temperature environments. It was found that even though these structures are significantly coarser than those made with other processing methods, they still exhibit comparable crack-growth resistance despite their lower strength. Toughening was induced by marked crack deflection as the crack path followed the metallic mortar phase coupled with significant crack bridging and brick pull-out in the image of the toughening mechanisms seen in nacre. These effects were shown to be more pronounced as brick size reduced closer to natural structures and additionally it was observed that crack growth resistance improved as a function of increasing temperature due to greater ductility in the metallic mortar.

To my family, for their unwavering support

Table of Contents

Abstract..... **1**

List of Figures ..... **iii**

List of Tables ..... **viii**

Acknowledgements ..... **ix**

Chapter 1: Introduction **1**

Chapter 2: Background **3**
2.1 Ceramics as Structural Materials..... 3
2.2 Inspiration from Nature..... 7
2.3 Nacre..... 8
2.4 Synthesis Methods..... 10
2.5 Coextrusion and Fibrous Monoliths..... 12

Chapter 3: Experimental Procedure **14**
3.1 Processing..... 14
3.2 Microstructural Characterization..... 16
3.3 Mechanical Characterization..... 17

Chapter 4: Optimization of Brick Morphology **20**
4.1 Results and Discussion..... 20
4.2 Summary..... 28

Chapter 5: Observations of Size Effects on Mechanical Behavior **29**
5.1 Results..... 29
5.2 Discussion..... 38
5.3 Summary..... 41

Chapter 6: Elevated Temperature Mechanical Properties **42**
6.1 Results..... 42
6.2 Discussion..... 47
6.3 Summary..... 49

Chapter 7: Conclusions and Suggested Future Work **50**

References **52**

List of Figures

2.1 Idealized stress-strain curves for a nominally brittle and ductile material. The brittle material has only a linear-elastic region before rupture failure while the ductile materials has a linear-elastic region followed by a region in which plasticity engages. The area under these stress-strain curves correlates to the damage tolerance and toughness, indicating that ductile materials like metals are much more damage tolerant than brittle materials like ceramics..... **5**

2.2 A load-displacement curve of a notched ceramic composite, showing a region in which "pseudo"plasticity occurs after the linear elastic region. This is a result of extrinsic toughening mechanisms inhibiting the crack propagation within the material, improving the damage tolerance in a similar fashion to the ductile stress-strain curve from **Figure 2.1**..... **6**

2.3 J-integral based *R*-curve showing the difference between a rising *R*-curve for damage tolerant materials and a flat *R*-curve that most brittle ceramics would exhibit. For flat *R*-curves, a singular value of *J*, which corresponds to the critical stress intensity, K_{IC}, is sufficient to describe the toughness of the material. While for ductile or damage tolerant materials that exhibit rising *R*-curve behavior, the stress intensity to propagate a crack rises as the crack extends into the material..... **7**

2.4 Fracture surface of nacre seen in a scanning electron microscope (SEM). The interlocking platelets or aragonite can be clearly seen, with the bio-protein mortar bonding the platelet “bricks” together..... **9**

2.5 Ashby property maps develop by [36] for the predicted behavior of synthetic brick-and-mortar materials. Real data composite and ceramet data is plotted as points while the synthetic models are shown as thick lines with arrows denoting the increasing aspect ratio of the bricks. Volume fraction of the mortar phase varies along the length of the curve as the thickness in the models is held constant. **10**

2.6 Nacre-like structures produced via freeze casting. The lamellar (**A**) structure resembles the as freeze cast layers produced via ice templating while a more brick-and-mortar (**B**) structure can arise through the compression of the freeze cast structure to reduce brick size and the amount of void space that eventually becomes filled with mortar [45]..... **11**

2.7 (**A**) honeycomb cross section of unidirectional of ZrB_2-30% SiC (cell) and graphite-15% ZrB_2 (boundary) fibrous monolith from [54]. The cellular structure resembles brick-and-mortar structures while (**B**) shows that the fracture behavior of FMs also have common toughening behavior to brick-and-mortar structures [64] with extensive crack deflection and bridging..... **13**

3.1 Schematic of the coextrusion assembly, showing how the core to shell ratio is maintained from a feed rod down to a filament..... **16**

4.1 Optical micrographs of the resulting Al_2O_3/10Ni metal compliant-phase ceramics: (**A**-**C**) single-pass coextrusions to 300 µm, specifically the *Sp-chop* structure (chopped and laminated in constrained die), *SP-lam* (chopped and pre-laminated into sheets), and *SP-45* (oriented filament laminated into sheets and consecutively offset 45° from the previous layer); (**D**-**F**) multipass coextrusions counterparts *MP-chop*, *MP-lam* and *MP-45*, that were extruded to 6 mm, then bound together and extruded again to 300 µm. The brighter phases are nickel metal while darker phases are the alumina..... **22**

4.2 Four-point bending data of the strength and initiation toughness of the six Al_2O_3/10Ni compliant-phase ceramic microstructures, as compared to that for the comparable monolithic Al_2O_3 standard. All the alumina structures containing the Ni compliant phase had a markedly lower strength, but were within 20-30 MPa of each other, the exception being the single-pass coextrusion material that was subjected to constrained lamination..... **24**

4.3 SEM micrographs showing the crack paths for all Al_2O_3/10Ni compliant-phase ceramic microstructures, post-failure from the notched toughness flexural test. Note that significant crack deflection can be seen in the *SP-chop* and *SP-45* samples (*SP-45* shows additional elastic bridging and some grain pull-out). These represent structures from the single-pass coextrusion while all the multipass structures (*MP* series) have relatively straight-through cracks with little to no evidence that the Ni mortar had any effect on the nature of the composite failure... **25**

4.4 (**A**) is before loading had begun with a clearly visible razor micronotch and (**B**) is after failure had occurred. Multiple crack paths can be seen deflecting around the individual bricks leading to crack bridging and brick pull-out, with failure occurring primarily along Al_2O_3/Ni boundaries, and brick failure within the inter layers that are oriented normal to the micro-notch..... **26**

4.5 Fracture-toughness R-curves, in terms of the stress intensity, K_J, back-calculated from nonlinear-elastic *J*-measurements (details given in the online Supplementary Information), comparing the *SP-45* offset structure with monolithic 25-µm grain-sized alumina [73] and freeze-cast SiC-PMMA brick-and-mortar composites [8] Results are also compared with a cellular Al_2O_3/20vol.%Ni composite [72] tested using double cantilever-beam specimens which allow for pronounced crack extensions due to their larger specimen widths. Our coextruded Al_2O_3/10Ni *SP-45* structure, however, can be seen display far superior *R*-curve toughness..... **27**

5.1 Optical micrographs of the three Al_2O_3/10Ni metal compliant-phase ceramics made with: (**A**) 500 µm filament, (**B**) 300 µm filament, and (**C**) 200 µm filament produced through coextrusion..... **31**

5.2 Four-point flexural strength for the three microstructures shows a ~45% increase with a 60% decrease in brick size from 500 to 200 µm. Corresponding crack-initiation K_{Ic} fracture toughness values increase by just over 20% for the same

decrease in brick size, indicating an improved overall mechanical performance as the brick-and-mortar structure is refined..... **33**

5.3 Crack-growth resistance curves measured using *in situ* three-point bend tests in the SEM. Results were obtained using nonlinear elastic fracture mechanics in terms of *J*, which were then converted into stress intensity K_J values (see Chapter 3). All three structures, with brick sizes varying between 200 and 500 μm, can be seen to exhibit rising R-curve behavior with K_J values exceeding 15 MPa.m$^{1/2}$; there is further a clear trend of steeper curves with decreasing brick size. Compared against these three structures is that of pure Al_2O_3 [73] which has a very shallow, almost flat R-curve..... **34**

5.4 Scanning electron micrographs of one of the 500 μm (**A**), 300 μm (**B**), and 200 μm (**C**) specimens after *in situ* fracture analysis. In the 500 μm specimen, crack deflection can be seen above and below the crack root, with minimal cracking through the bricks. While the 300 μm specimen shows significantly more crack deflection above the crack root with noticeable crack bifurcation and crack bridging this is region. Finally, in the 200 μm sample the crack deviates somewhat from the plane of maximum tensile stress as there is extensive mortar delamination and crack deflection as well as multiple bricks bridging the crack path..... **36**

5.5 SEM micrograph of a 300 μm specimen showing the extent of interfacial delamination in the crack wake. While the inclusion of a metallic mortar was intended as a means of introducing a ductile failure mechanism into the structure, when weak interfaces are present there is little evidence of plasticity in the failure region and the crack travels along the interface instead. This behavior is inherent in all three structures produced by this method..... **37**

5.6 A plot of the linear elastic solutions of He and Hutchison [75] which show the conditions where a crack impinging normally on a dissimilar material interface between materials 1 and 2 will either penetrate the interface or arrest/deflect along the interface. For a ~90° incident crack angle, two factors determine whether or not the crack will penetrate: (i) the elastic mismatch between the two materials which is given by the first Dundurs' parameter $\alpha = (E_1 - E_2)/(E_1 + E_2)$, where E_1 and E_2 are the Young's moduli of the two materials [77], and (ii) the ratio of the interfacial toughness to the toughness of material 2 which the crack would enter if it penetrated the interface, $\mathcal{G}_{c,interf}/\mathcal{G}_{c2}$. For a penetrating crack originating in the alumina traveling into the nickel mortar, $\alpha \sim -0.26$. If cracks emanating from Vickers hardness indents in the alumina are directed to impinge normally on the nickel/alumina interface, as the right-hand micrograph shows they do not penetrate the interface but rather form delamination cracks along the interface. This allows for the estimation of an upper-bound toughness of the nickel/alumina interface of $\mathcal{G}_{c,interf} \sim 0.23$..... **38**

5.7 Comparison SEM micrographs imaged using secondary electron (SE) imaging (**A**) and backscatter (BSE) electron imaging (**B**) showing the presence of a region between the alumina bricks and nickel mortar. Backscatter images (**C**) show that the cracks traverse along the interface between the reaction region and the nickel mortar; higher-resolution imaging (**D**) indicates that the region is comprised of alumina grains with the nickel in the grain boundaries providing the higher elemental contrast with BSE. This is likely a remnant of the decomposition reaction that occurs during the final heat treatment to reduce the nickel aluminate spinel formed during sintering back into nickel and alumina..... **41**

6.1 Flexural strength produced via 4-point bending of the 45° offset brick-and-mortar structure produced with 200 µm filament. Strength gradually increases from room temperature to 600°C, likely due to reduction of residual stresses from Al_2O_3 and Ni thermal expansion mismatch, while a decrease in strength is seen after 700°C with the drop in strength accelerating after 800°C..... **44**

6.2 *R*-curves the coextruded brick-and-mortar structure at room temperature, 600, 700, 800, and 900°C. Room temperature and 600°C have almost identical curves, with a small increase at 700°C. This is followed by a marked increase at 800°C where ductile mortar behavior is believed to engage instead of interfacial mortar/brick failure. The *R*-curve then drops again at 900°C, with correlates with a significant drop in strength from **Figure 6.1**, meaning that the temperature has compromised all mechanical properties at that point..... **45**

6.3 *R*-curves produced at room temperature for the same 200 µm coextruded structures, one with in *in-situ* SEM method used in the previous chapters while the lower curve is produced with the indirect method that uses compliance evolution to determine the crack length. The indirect method has a noticeably lower curve, which is due in part to microcracking that occurs during the unloading cycle necessary to determine the change in compliance. Microcracking during unloading will extend the Δa, which extends out the curve, lowering it in comparison to the *in-situ* method that the crack length at the exact point in load that it extends. This produces a more conservative curve, but because all the *R*-curves in **Figure 6.2** are measured using the method, the comparisons are self-contained and valid..... **46**

6.4 Crack pathways from fracture toughness specimens seen at each of the elevated temperatures. Both the 600°C and 700°C samples had fracture pathways that were identical to room temperature pathways seen in the last chapter, with the crack either failing through bricks or along the brick-mortar interface. The specimens at 800°C and 900°C can be seen to have cracking within the nickel mortar which corresponds to the larger increase in *R*-curve behavior seen in **Figure 6.3**..... **47**

6.5 Scanning electron images taking in backscatter electron (BSE) imagining mode to enhance the contrast between the Al_2O_3 bricks and Ni mortar of samples broken at 800°C. (**A**) and (**B**) show cracks contained within the mortar, with little to no interfacial cracking being present. (**C**) and (**D**) have evidence of ductile tearing and bridging of the crack passing through the mortar..... **49**

List of Tables

4.1 Microstructural information for the six Ni compliant-phase ceramic structures, shown in **Figure 4.1** and developed by single and multipass coextrusion in this study..... **23**

5.1 Microstructural information for the three Ni compliant-phase ceramic structures, shown in **Figure 5.1** and developed by coextrusion of different filament diameters..... **32**

5.2 Tabulated data for the interfacial toughness, determined using the He-Hutchinson analysis..... **38**

Acknowledgements

First and foremost, I would like to thank my advisor, Professor Robert O. Ritchie for his mentorship over the five years in which I have been a student at UC Berkeley. Prof. Ritchie is an outstanding advisor, encouraging me to pursue my own interests while also sharing his wealth of expertise. It was an honor and an amazing opportunity to have worked with him.

I would also like to thank Dr. Bernd Gludovatz for sharing his expertise not only with equipment, but also with the methods I would later rely on.

This research required extensive use of facilities provided by the Ultra-High Temperature Ceramics (UHTC) group at my undergraduate institution, the Missouri University of Science and Technology. I am extremely grateful to my former research advisor, Professor Greg Hilmas, for not only providing me full access to the facilities at Missouri S&T, but also with providing expertise on the complicated ceramic processing necessary for this project. I would also like to thank Professor Jeremy Watts for spending countless hours of his time helping me: between process troubleshooting, mechanical testing, and my persistent questions.

Finally, I would like to thank my family for their steadfast support in my endeavor to pursue a PhD at Berkeley. I would never have been able to achieve this without them.

This work was supported by the Mechanical Behavior of Materials Program (KC-13) at the Lawrence Berkeley National Laboratory, funded by the U.S. Department of Energy, Office of Science, Office of Basic Energy Sciences, Materials Sciences and Engineering Division, under contract no. DE-AC02-05CH11231.

Chapter 1
Introduction

In many respects, ceramics represent ideal lightweight materials in terms of their high specific strengths, elastic moduli and creep resistance, coupled with low thermal expansion and good chemical resistance although, as is widely appreciated, their adoption for the vast majority of structural applications has been severely compromised by their low toughness and ductility, a product of strong bonding and a high Peierls stress, which makes them highly flaw-sensitive. Nature, however, is remarkably adept at using brittle, ceramic-like, materials for many of its structural applications. Sea shells are a notable example in that they can display excellent strength, toughness and even wear resistance despite consisting primarily of a brittle mineral, *e.g.*, aragonite in the nacre layer of abalone shells [1-3]. The obvious success of Nature in this regard has led to an entirely new field of research endeavor, that of biomimetics, resulting in an increasing scrutiny of the structure of natural materials, such as sea shells, fish scales, bamboo, bone, teeth, and so forth, for inspiration in the design of new and improved lightweight structural (and functional) materials.

Despite a small palette of constituent materials to work with, most with meagre mechanical properties, Nature attains remarkable properties and functionality by designing hybrid materials, often comprising soft and hard phases, which are assembled into a hierarchical architecture, spanning multiple length-scales, containing graded interfaces and ingenious gradients in structure, orientation and/or composition. Whereas this presents a compelling landscape for bio-inspiration, the problem in mimicking such complex hierarchies in a man-made material is in our latent inability to process them. The "top-down" fabrication/engineering approaches that are regularly used to make bulk structural materials are simply not practical for building multi-scale structural architectures with the same degree of organization as biological materials where "bottom-up" growth and adaptation are utilized. However, the development of certain materials processing technologies show promise in this regard; methods such as 3-D printing and freeze-casting are capable of making relatively large parts yet, in principle, can enable fine structural control even down to the nanoscale.

To date, significant research [4-10] has been devoted to the synthesis of bio-inspired ceramic hybrid materials, mainly in the image of the "brick-and-mortar" structure of nacre. Nacre is a highly efficient natural material in that, in energy terms, it displays a toughness which is over three orders of magnitude larger than that of its constituent phases, *i.e.*, 95 vol.% of aragonite mineral "bricks" separated by a biopolymeric "mortar".

This study will focus on a new method of producing biomimetic nacre, specifically with low metallic mortar content. A concept that has been predicted to have the most ideal mechanical properties, but also one that has eluded research groups because of a host of difficulties arising from the incompatibility with metal and the current suite of processing methods being used to synthesize these structures. The first part of the study will focus on how to manipulate this technique, coextrusion, to produce optimal microstructures in regards to mechanical properties. This will be done using image analysis, as well as advanced mechanical testing to correlate microstructural differences with mechanical performance. The second and third parts of this

study will further investigate the optimization of coextruded brick-and-mortar structures to see the full engagement of the inherent intrinsic and extrinsic toughening

Chapter 2
Background

2.1. CERAMICS AS STRUCTURAL MATERIALS

As society and technology advances, the constituent materials for these technology must advance alongside them. This is especially true for structural materials, which are used primarily for their mechanical properties such as strength, toughness, and hardness. Structural materials are used everywhere: from the steel and concrete that comprises the majority of our infrastructure, to the composites and aluminum that our airframes are built from. Within this class of materials, metals have long dominated due to an excellent combination of factors. They tend to have excellent mechanical properties in terms of strength and toughness as well as exhibiting plasticity instead of catastrophic failure that increases their factor of safety and reliability in applications where long time use is needed. Furthermore, they are easily available with a wide range of tunable properties because of their ability to alloy with other metals and heat treatment cycles to maximize mechanical performance. Combining this all with their ability to be formed and machined in a variety of complex shapes makes them a difficult candidate to contend with for future materials.

However, certain aspects of metals have inhibited their usability in specific functions. Most metals are relatively high density, with notable exceptions being aluminum and titanium at 2.7 g/cm^3 and 4.5 g/cm^3 respectively, compared to steel which sits between 7.75 and 8.05 g/cm^3. Applications where weight is an important factor like armor or spacecraft superstructures, are therefore limited to a much smaller range of metals to even be considered. Additionally, high temperature environments such as hypersonic control surfaces, jet engines, and power turbines are operating at temperatures beyond what many metals can withstand. This has severely limited the options of available metals to a handful of super alloys and refractory metals. The issue is exacerbated even further as engine and turbine environments move to higher operating temperatures to improve their fuel efficiency. Finally, most metals tend to be quite susceptible to corrosion due to the thermodynamic favorability of metal oxides over their pure metallic counterparts. Corrosion deteriorates the mechanical performance through not only the removal of material [11,12] which increases the load bearing stress on the remaining cross-section, but also through a process called stress corrosion cracking [13,14], in which oxides form at crack tips, fail in brittle manner, and then exposes new metal at the crack tip that can be oxidized. This combination of properties has lead researchers to start looking elsewhere for a new class of high performance structural materials for increasingly hostile environments and tighter weight restrictions.

Ceramic-based materials provide a host of ideal properties to potentially compete with metals in these spaces. Ceramics are a group of inorganic materials that are comprised of covalently or ionicly bonded atoms generally grouped in the oxide, carbide, boride, or nitride family. This high directional bonding leads to structures that are on average 3-6 g/cm^3, which competes well with the lightest of metals. Additionally, the bonding in ceramic materials is very strong, if not too strong; and therefore the strengths can range from a couple hundred MPa, all the way into the GPa range which far exceeds the yield strength of any metals. In the case of oxide ceramics,

because they are already oxidized, they tend to be extremely corrosion resistant and do not experience they same stress corrosion cracking prominent in metals. Tying all of this together is that almost all ceramics have substantially high melting points, which can range from the low 2000°C all the way beyond 3000°C in the case of the some ultra high temperature carbides and borides. This allows for maximum mechanical operating temperatures to far exceed that of the Ni-based superalloys in use today.

Ceramics and ceramic-based composites are not perfect however, and are plagued with a handful of backbreaking flaws that have limited their adoption into fields still dominated by metals. **Figure 2.1** shows an idealized stress-strain curve for a typical brittle material and a typical ductile material. Ceramics exhibit brittle failure, in which once a crack starts to propagate, it will proceed to extend through the material, leading to total failure of the material. Metals on the other hand exhibit ductile failure, where plastic deformation allows for strain energy relief in the form of yielding and hence the materials do not fail catastrophically. This is paramount when designing technology incorporating a material: if the engineered strength is exceed, can the material withstand some amount of damage? In the case of most ceramics this is not possible, while metals will yield plastically instead, leading to damage tolerance. Damage tolerance can be visualized and calculated by taking the area under the stress-strain curve and it becomes immediately apparent that the brittle ceramic has little damage tolerance in comparison to the ductile metal.

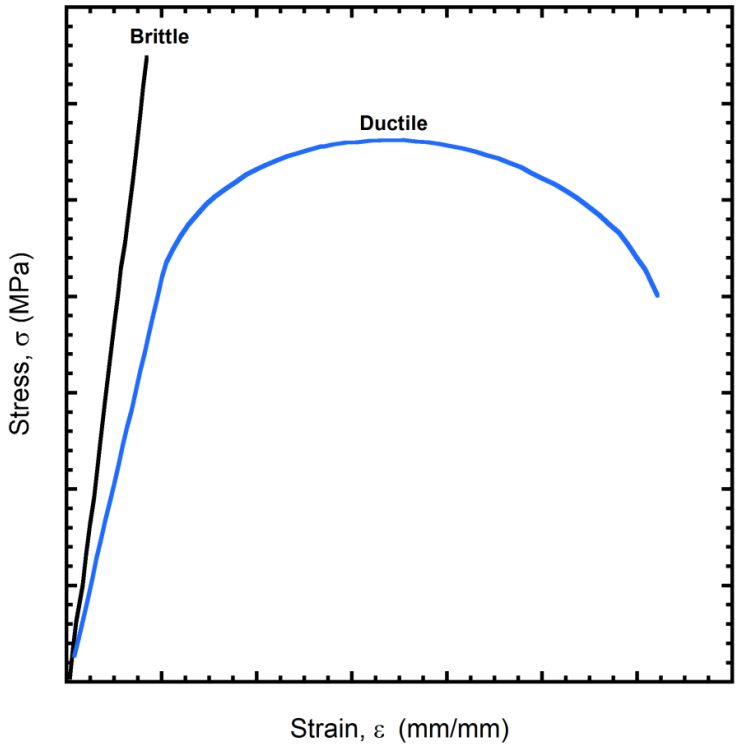


Figure 2.1: Idealized stress-strain curves for a nominally brittle and ductile material. The brittle material has only a linear-elastic region before rupture failure while the ductile materials has a linear-elastic region followed by a region in which plasticity engages. The area under these stress-strain curves correlates to the damage tolerance and toughness, indicating that ductile materials like metals are much more damage tolerant than brittle materials like ceramics.

The origin of this low damage tolerance is due to ceramics having exceptionally low toughness values, with little crack growth resistance developing as well. This is widely regarded as one of the major conflicts between strength and toughness [15], as these properties tend to be mutually exclusive because of how bonding plays a pivotal role as the origin of both properties. Indeed, the strong bonding that leads to the high strength values in ceramics is also detrimental in regards to fracture toughness, as it cannot support dislocation movement that metals are able to capitalize on. Therefore, when a metal reaches its yield strength it is able to deform plastically as a form of stress relaxation which blunts crack tips and reduces the stress concentration. Conversely, polymers which have extremely high degrees of plasticity are very tough but in comparison their strengths tend to be drastically lower than metals or ceramics because of the weaker chemical bonding and structure present in them. While a ceramic is only able to permanently break bonds and as a way to mitigate fracture energy at the crack tip. In most ceramics the newly forming crack is able to transverse the material unimpeded. However, some ceramic materials are able to capitalize on a variety of extrinsic toughening mechanisms to arrest crack propagation in the material, allowing them to exhibit non catastrophic failure and producing stress-strain profiles reminiscent of ductile materials as seen in **Figure 2.2**. Transformation toughening, crack bridging, crack deflection, and crack wedging are all forms of extrinsic toughening mechanisms that can be engineered into ceramic materials to improve mechanical performance as a form of crack growth resistance that occurs behind the crack front.

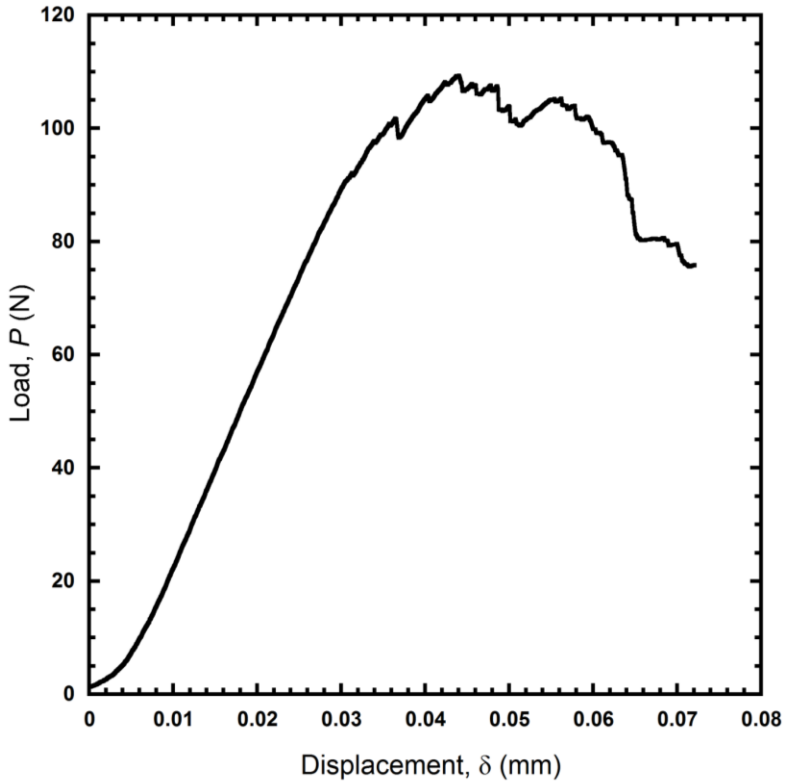


Figure 2.2: A load-displacement curve of a notched ceramic composite, showing a region in which "pseudo"plasticity occurs after the linear elastic region. This is a result of extrinsic toughening mechanisms inhibiting the crack propagation within the material, improving the damage tolerance in a similar fashion to the ductile stress-strain curve from **Figure 2.1**.

Crack growth resistance can be quantified and visualized in a resistance curve (*R*-curve), and is vital when comparing damage tolerant materials [16]. Brittle materials are generally not represented with *R*-curves as a critical singular value of toughness (K_{IC}) is enough to describe the entire regime of toughness in the material. This can be denoted with what is called a flat *R*-curve as seen in **Figure 2.3**, and shows that for any value of crack length (Δa), the same critical stress intensity is needed to propagate said crack at any length. The counter to flat *R*-curves is that of a rising *R*-curve, also shown in **Figure 2.3**, which is what happens when a material increases its toughness while a crack is extending through it. Ductile materials such as metals exhibit rising *R*-curve behavior naturally, as plastic behavior in front of a crack tip acts as a form of intrinsic toughening through crack blunting and strain relaxation [17]. Ceramics that exhibit extrinsic toughening effects are also able to produce rising *R*-curves, as propagating cracks will be inhibited by mechanisms engaging in the wake of the extending crack [18-21]. Therefore, the ideal structural ceramics will exhibit rising *R*-curve behavior similar to metals, as it will be indicative of damage tolerance and non catastrophic failure.

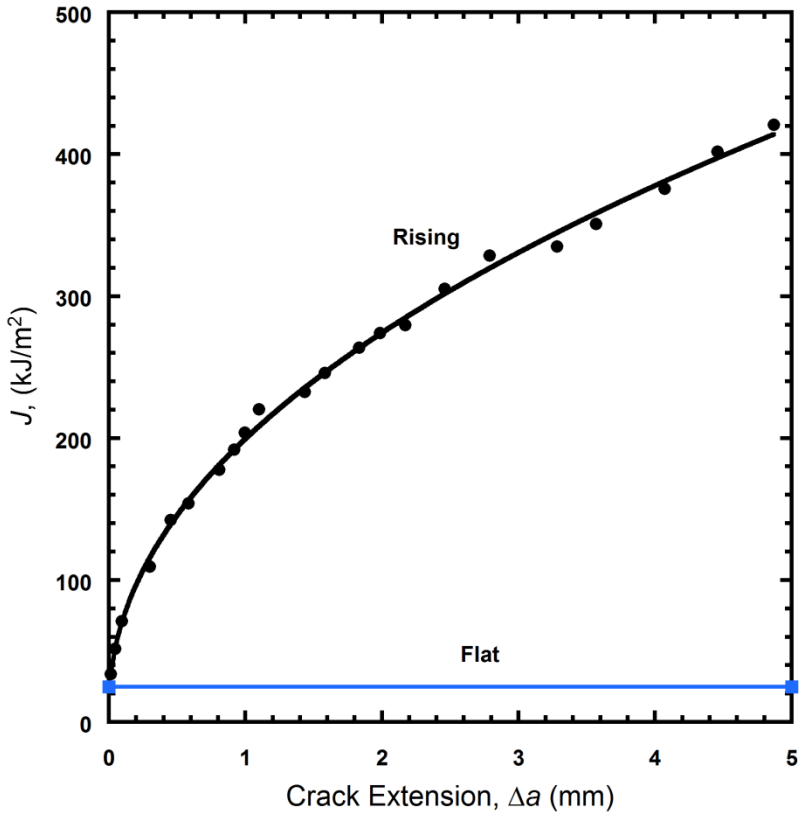


Figure 2.3: J-integral based *R*-curve showing the difference between a rising *R*-curve for damage tolerant materials and a flat *R*-curve that most brittle ceramics would exhibit. For flat *R*-curves, a singular value of energy release rate, which corresponds to the critical stress intensity, K_{IC}, is sufficient to describe the toughness of the material. While for ductile or damage tolerant materials that exhibit rising *R*-curve behavior, the stress intensity to propagate a crack rises as the crack extends into the material.

2.2. INSPIRATION FROM NATURE

As it was mentioned earlier, in most synthetic materials the properties of strength and toughness are often mutually exclusive [15], but there are numerous examples of naturally-occurring materials that take advantage of a hard brittle constituent for strength yet still achieve excellent fracture resistance in the form of unusual combinations of strength and toughness [22-24]. Many of these materials, such as nacre, dentin and bone, are made primarily of a brittle mineral ceramic, such as aragonite or hydroxyapatite, and a soft biopolymer, such as cellulose, lignin, chitin or collagen, which is combined into a complex hierarchical microstructure, with different properties originating at different length-scales – strength at the nanoscales and toughness, additionally, at much coarser scales [1,15]. In contrast to many monolithic ceramics where catastrophic (unstable) fracture generally ensues, these natural biocomposites can sustain the subcritical extension of cracks, *i.e.*, they can develop toughness during crack growth which is displayed in the form of rising *R*-curve behavior; in other words they can generate fracture resistance via both intrinsic and extrinsic mechanisms and as such "defeat" the "conflict" between strength and toughness [15].

These natural biocomposites come in a variety of different designs, but each can provide insight into synthetic material design because of the unique ways they develop toughness and strength in lieu of high performance constituents. Take for example the natural dermal armor present in most fish as scales and in many terrestrial animals as well [25-27]. The ganoine scales of the alligator gar consist of a hard ceramic phase (hydroxyapatite) in the form of rods which are bound together via a network of collagen fibers. The hydroxyapatite provides strength and hardness necessary for protecting against attack while the collagen fibers give toughness and flexibility to the scales: a marriage of two dissimilar materials to mitigate the inherent mechanical weaknesses of each constituent [24,28]. There are other examples of natural structural materials used in much higher stress or higher cycle environments, respectively the dactyl club of the mantis shrimp or the bones that makes up our own bodies. The dactyl club of the mantis shrimp is designed for high velocity strikes that can shatter hard shells of mollusks and crustaceans making it an offensive weapon which undergoes repeatedly high compressive stresses. Hydroxyapatite is once again present in the hard mineralized strike face of the organ, while it is supported by helicoidal architecture of mineralized chitin that minimize the internal damage by deflecting microcracks and crack shielding not dissimilar to many ceramic fiber reinforced composites [29-31]. Bone is arguably an even more complex hierarchical composite which consists of more brittle constituent than either of the two previous examples and sees a high cycle fatigue environment through the course of its lifetime. Collagen molecules are embedded with hydroxyapatite crystals which comprise larger mineralized collagen fibrils that are crosslinked to one another. These fibrils make up larger fiber arrays that surround osteon canals that are further surrounded by heavily mineralized cement lamellae structure. This leads to complex extrinsic and intrinsic fracture behavior between extensive crack deflection, ligament bridging, sliding, and plastic deformation of the collagen network [32-34]. The common theme throughout these structures is their reliance on a mineral phase to provide strength while the structure and biopolymeric phase provide the necessary toughness.

2.3. NACRE

Of particular interest for the development of damage tolerant ceramics is the structure of certain mollusk shells, specifically the nacre layer in red abalone. Unlike the previously mentioned biomaterials, nacre is unique in that it is comprised almost entirely of the ceramic phase at 95 vol. % aragonite ($CaCO_3$) platelets (~0.5 μm thick, 5-7 μm wide) that are bonded together with thin layers of bio-proteins in a "brick-and-mortar" arrangement as seen in **Figure 2.4**. The nacre structure, which has become the "gold standard" for biomimetics, generates strength from the mineral platelets, but also displays exceptional toughness that can be three orders of magnitude higher (in energy terms) than either the mineral or bio-polymer; this is achieved through limited inelastic deformation in the bio-polymer mortar, which acts as a compliant (mortar) layer [1-3,22,35].

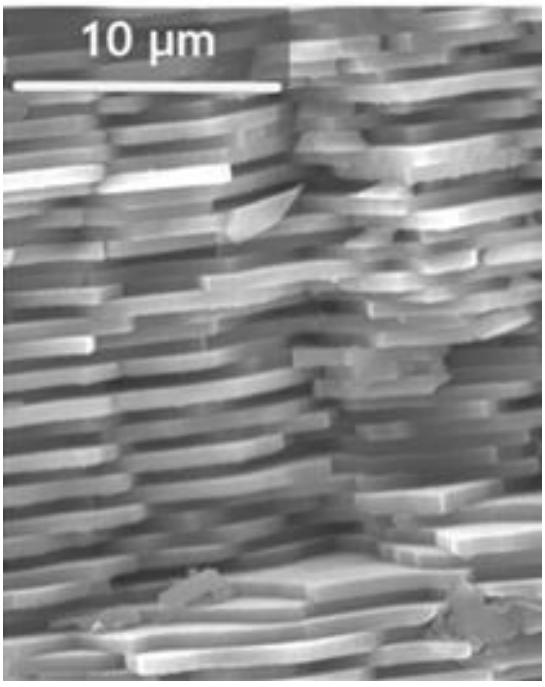


Figure 2.4: Fracture surface of nacre seen in a scanning electron microscope (SEM). The interlocking platelets or aragonite can be clearly seen, with the bio-protein mortar bonding the platelet "bricks" together.

The mechanical behavior of nacre has been widely modeled [35-41], with several key factors arising that are helping to guide the development of synthetic brick-and-mortar composites. Vertical interfaces provide an important role in the composite stiffness as well as the failure behavior, therefore suggesting that the ceramic brick phase cannot have too high of an aspect ratio or behavior will mimic that of a layered laminate composite. Additionally, brick size and aspect ratio is tuned to the mortar, brick, and bond strength; and that for increasing mortar yield strength the optimal brick size decreases. This means that low yield strength polymeric mortars would therefore need much larger bricks than a higher yield strength metallic mortar. To that end, metallic mortars are modeled to have much higher work of failure and could lead to outliers that defeat the conflict of strength and toughness. These things can be visualized in an Ashby plot reproduced from [36] in **Figure 2.5**, notably showing the modeled Al_2O_3/Al and Al_2O_3/Ni

systems. The nickel based mortar is expected to have improved work of failure due to the higher modulus and failure strain. The summation of several of these models for the design of synthetic brick and mortar materials is that they:

- Have low (<10 vol.%) mortar content to maximize on the composite strength provided by the strong brick phase
- Have large brick aspect ratios, ideally tuned to the mechanical properties of the mortar and brick phase while not being too large to bypass vertical mortar rupture
- Will have mortar that can deform plastically to engage in intrinsic toughening before rupture while allowing extrinsic structural toughening
- Can contain either polymeric or metallic mortar, with metallic mortar expected to produce the best mechanical properties in regards to strength and toughness

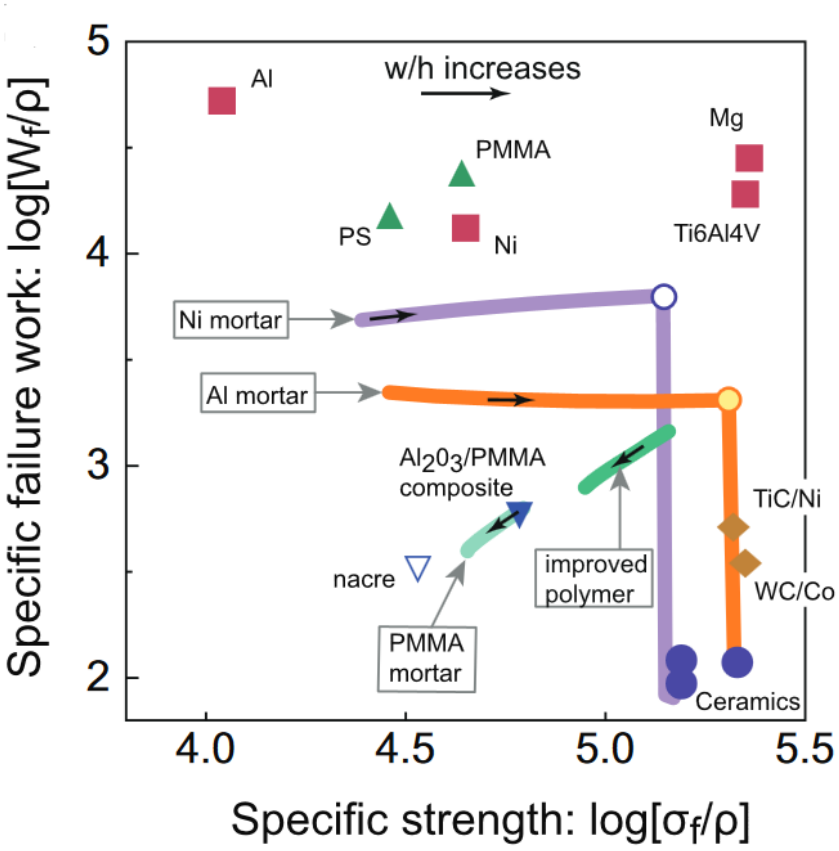


Figure 2.5: Ashby property maps develop by [36] for the predicted behavior of synthetic brick-and-mortar materials. Real composite and cermet data is plotted as points while the synthetic models are shown as thick lines with arrows denoting the increasing aspect ratio of the bricks. Volume fraction of the mortar phase varies along the length of the curve as the thickness in the models is held constant.

2.4. SYNTHESIS METHODS

2.4.1. Freeze Casting and Ice-Templating

In the continuing race to develop synthetic brick-and-mortar structures, freeze casting (ice templating) has garnered significant interest, with many papers being published to date with promising results. The ceramic phase is dispersed in water to form an aqueous suspension that is directionally frozen, which produces unidirectional sheets of ice in the suspension, expelling the ceramic powder in the process. After the freezing is complete, a layered structure of ice and ceramic remains, which can then be subsequently freeze dried to leave a scaffold of ceramic layers. This scaffold is sintered to densify the ceramic layers, and from here the compliant mortar phase is infiltrated to form the final brick-and-mortar structure [6,8,9,42-44]. In some cases the scaffolds undergo cold pressing to reduce the void space that will eventually be filled with mortar while also fracturing the lamellae into smaller bricks [45,46]. Structures produced this way can be seen in **Figure 2.6**, showcasing the nacre-like ceramic hybrid material with damage-tolerant properties. This "top-down" design approach has several inherent advantages that make it an attractive method for future research. The method is highly tunable, being able to produce varying lamellae thicknesses and surface textures that translate into brick aspect ratio as well as improved brick sliding resistance. Ice-templating also allows for the production of larger volumes of samples as it is considered a bulk technique with increased throughput that is difficult to mimic with many of the methods that will be discussed later.

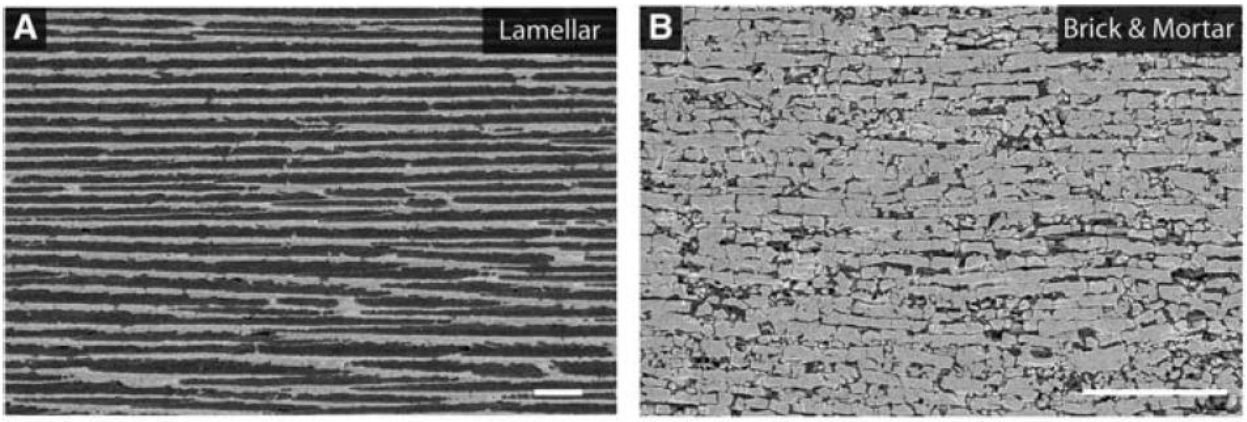


Figure 2.6: Nacre-like structures produced via freeze casting. The lamellar (**A**) structure resembles the as freeze cast layers produced via ice templating while a more brick-and-mortar (**B**) structure can arise through the compression of the freeze cast structure to reduce brick size and the amount of void space that eventually becomes filled with mortar [45].

However, the nature of freeze casting also leads to some detrimental conditions that continue to limit its usefulness for the future advancement of synthetic brick-and-mortar structures. Because of the necessary void space needed for complete infiltration, ice-templating has not been able to achieve high ceramic volume fractions (typically not above 80%), and the corresponding fractions of the compliant phase are too high for optimum properties; as such, they do not truly mimic natural nacre. Additionally, the most significant experimental results have involved polymeric compliant phases, whereas theoretical modeling [36] suggests that the adoption of a metallic mortar would result in even better combinations of strength and toughness. However,

infiltrating a metallic phase into a ceramic scaffold is inherently difficult due to poor wetting between many of the ceramic-metal combinations of interest, such as alumina and nickel. Only a few studies have able to successfully infiltrate metal into freeze cast structures, with ceramic contents around 50 vol.% at the lowest, which is significantly worse than any of the successful polymeric mortar systems. Correspondingly, fine-scale, brick-and-mortar structures with high ceramic content and a metallic compliant phase, which are predicted [36] to display optimal damage-tolerance, have yet to be made using freeze-casting techniques.

2.4.2. Self-Assembly and Bottom-Up Approaches

Since nacre itself grows in a layer by layer fashion, other design approaches for synthetic brick-and-mortar structures are taking inspiration not only from the structure but also from how it is generated. To this end, bottom-up approaches in which the mortar and bricks are combined at the same time are gaining more traction in lieu of back infiltrating preformed structures. This presents a significantly more difficult challenge, since with freeze casting one part of the process can be focused on at a time to optimize the final result, while bottom-up approaches require all these moving parts to come together at the same time to form the intended structure. A quick overview of some of these methods include the functionalization of graphene oxide and then allowing it to deposit layer by layer using sedimentation [47], or the evaporation induced self-assembly of alumina platelets with polymeric mortar [48]. Other self-assembly methods include the use of vacuum as a driving force [49] or building the structure layer by layer manually on a substrate [50]. Some new techniques are also taking advantage of lessons learned from ice-templating, such as using it is as a method to orient platelets in a suspension that already contains both the brick and mortar precursors [51]. This uniquely combines the bulk capabilities of freeze casting while also self-assembling the completed structure without any need of infiltrating a mortar, bypassing wetting issues and allowing for precision control of the mortar to brick volume percentages. A similar method that uses magnetically assisted slip casting as the driving force for self-assembly has also shown promising results into production of brick-and-mortar structures [52].

As with freeze casting, there are still issues that have to be addressed with these bottom-up approaches. The most notable drawback is the limited sample volume, with many of these synthetic structures being incredibly thin, which makes mechanical testing much more difficult as well as restricts the material from potential engineering applications. Furthermore, the techniques are not nearly as tunable as freeze casting, restricting the materials that can be used for the brick or mortar. Continuing on this thread, most of the mortar that has been seen in these materials have been polymeric in nature, with the notable exception being the magnetically assisted slip cast structures. This compatibility issue that arises between metals and ceramics is a persistent limitation in self-assembly techniques and the back infiltration necessary for the freeze casting.

2.5. COEXTRUSION AND FIBROUS MONOLITHS

Considering the drawbacks of freeze casting and self-assembly, this body of work will look to a different ceramic processing technique to bridge the gap into metallic compliant phase brick-and-mortar structures. Coextrusion is a technique that has been used for years as a method of forming unique composites called fibrous monoliths (FMs) [53-57]. FMs are similar to other fiber-reinforced composites, and show similar crack deflection and propagation behavior under specific loading conditions. They consist of either ceramic-ceramic or ceramic-metal architectures with a distinct cell and cell boundary made respectively of each material. In the case of FMs, the cell acts as fiber while the cell boundary acts as the matrix phase between these fibers, leading to improved toughness and non-catastrophic fracture behavior [58-63]. Coincidentally, the cross sections of these materials normal to the fiber direction are similar to that of a brick-and-mortar composite (**Figure 2.7**), and exhibit fracture behavior similar to the extrinsic toughening found in brick and mortar structures. Most FMs are unidirectional in the orientation of their cellular structure to more closely mimic fiber reinforced ceramics such as SiC_f/SiC_m, but there is still potential for multidirectional structures.

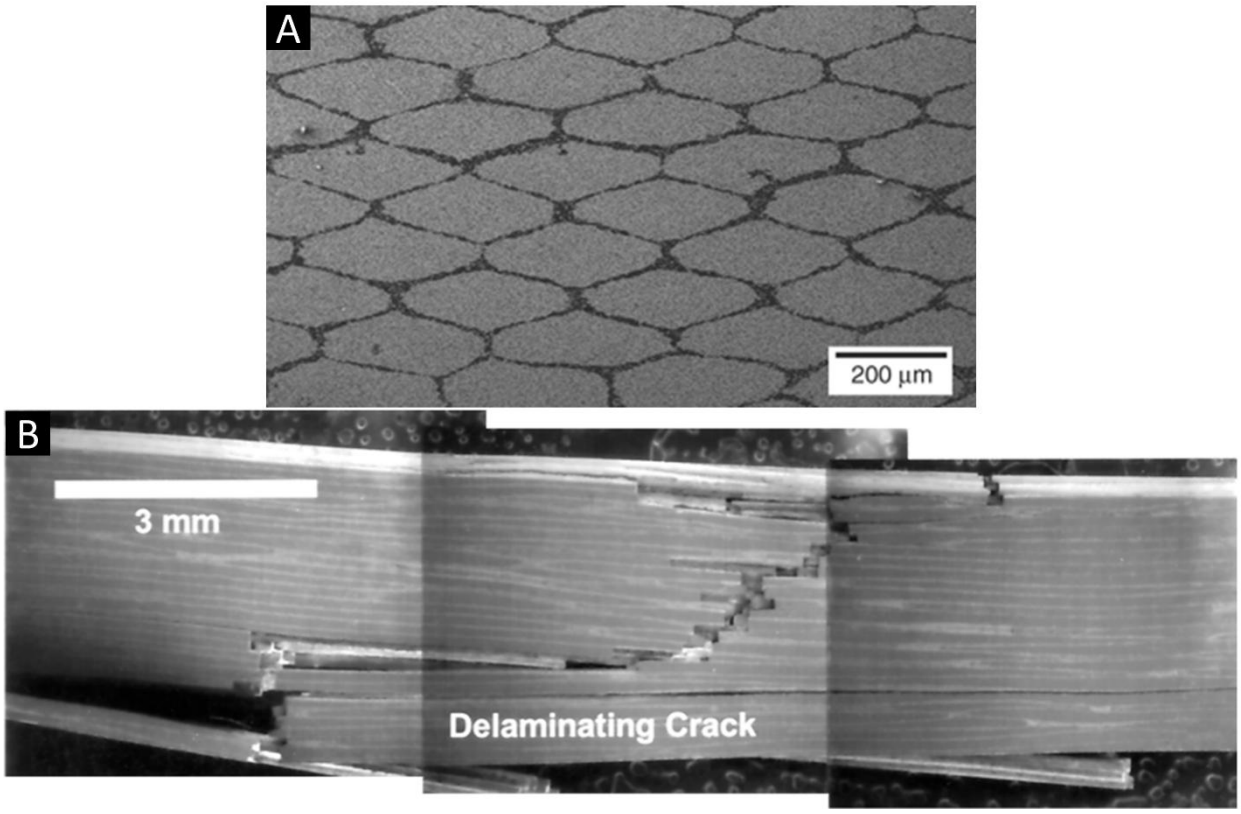


Figure 2.7: (**A**) honeycomb cross section of unidirectional of ZrB_2-30% SiC (cell) and graphite-15% ZrB_2 (boundary) fibrous monolith from [54]. The cellular structure resembles brick-and-mortar structures while (**B**) shows that the fracture behavior of FMs also have common toughening behavior to brick-and-mortar structures [64] with extensive crack deflection and bridging.

The fabrication of coextruded fibrous monoliths is a somewhat involved process that takes time and patience. Initially, core material and shell material are each mixed into separate

thermoplastics at a high solids loading (>50 vol. %) of ceramic to take advantage of the easy formability and malleability of the polymer. A feed rod of material is produced with a very specific core and shell diameter, while the core to shell ratio is preserved through extrusion as the cross section of the rod is reduced down to a filament. In the case of FMs this filament is aligned and laminated together, forming the iconic honeycomb structure seen in **Figure 2.7**. The thermoplastic is then slowly pyrolyzed out before final sintering, leaving a dense structure with a heterogeneous structure with discrete cell and boundary phases. However, this method can potentially be modified to produce brick-and-mortar microstructures. It is this core/shell filament that can be sectioned into individual pieces, and therefore processed as if it was an individual "brick" in the brick-and-mortar structure. The advantages to developing synthetic brick-and-mortar material is that coextrusion allows for precise control of the mortar content, including low volume of mortar by simply adjusting the shell thickness of the feedrod. Additionally, it is a bulk method that should be able to work with a metallic mortar phase, and mimics the advantages of the bottom up self-assembly techniques by including the mortar throughout the whole process instead of attempting to infiltrate it after the fact. Not only can coextrusion be used to produce some of the first low metallic content brick-and-mortar structure, but the structures produced this way can provide insight into the continued modeling and development of this new class of ceramic microstructures.

Chapter 3
Experimental Procedures

3.1. PROCESSING

Brick-and-mortar hybrid alumina ceramics were produced through coextrusion of ceramic and thermoplastic mixtures. Initially, polyethylene-ethyl acrylate (EEA; melt index 20, Dow Chemical) binder was softened above its glass-transition temperature in a high-shear rheometer mixer (Plasti-Corder, C.W. Brabender) to a temperature of 150°C. Alumina (A-16-SG, Almatis) with 4 vol.% ZrO_2 (3YSZ, Tosoh) was incorporated into the EEA until a volume fraction of 55 vol.% solids was achieved while the rheology was controlled through minor additions of heavy mineral oil (HMO; Sigma Aldrich). This powder/binder mixture was then molded into a cylindrical core (20.4 mm) using a heated die and hydraulic ram. The process was then repeated with NiO (-325 mesh, Alfa Aesar) to form a separate powder/binder mixture which was subsequently pressed into two half pipe shells (130°C, 10 tonnes, ~1 mm thick) and then laminated around the core which forms the core/shell extrusion feed rod. A mortar/shell ratio of 82.5/17.5 was chosen based off of the known volume reduction of NiO to Ni that would occur during sintering, leaving a final quantity of 10.2 vol.% of Ni within the structure. The feed rod was extruded through a heated spinneret (~135°C) to form a 300 μm filament maintaining the same core-shell ratio (82.5/17.5) throughout the newly produced filament's cross section (**Figure 3.1**). To aid in the orientation of filament after extrusion, the filament was tightly wound around a spool to form a ribbon which was then bonded with a spray adhesive before being sliced off as an oriented sheet of filament, allowing for easy manipulation of the filament for either chopping or laminating.

To ascertain the relationship between filament manipulation and brick morphology, a series of samples were produced using single-pass (termed "*SP*") coextrusion with the 300 μm filament. Chopped filament (~500 μm in length) was poured into a 25 mm x 45 mm steel die and laminated to form a billet of randomly oriented filament bricks, termed as "*SP-chop*", as the first series of samples. To increase the bricks' aspect ratio through free lateral deformation, chopped filaments were spread out, compressed into sheets and laminated together in the same steel die to form a billet to produce the second series, "*SP-lam*". A third sample series, "*SP-45*", was created by cutting rectangles from the filament ribbon, either perpendicular, parallel, or 45° to the filament direction, which were then stacked and laminated together (model G50, Wabash MPI) so that each layer was 45° clockwise from the layer beneath. In an attempt to reduce the brick size in each of these three structures, a parallel series of samples was produced by multipass coextrusion, termed "*MP*", by laminating twelve filaments from an initial 6-mm extrusion into a new feed rod that was further extruded to 300 μm, from which the same three sample series were made (termed *MP-chop*", "*MP-lam*" and "*MP-45*").

Two additional series were produced with the same processing conditions as the *SP-45* for the studies involving brick size effects and temperature effects. In one of these series the feed rod that was extruded through a 500 μm spinneret to produce 500 μm filament, and in the other series the feed rod was extruded through the same 300 μm spinneret while also being drawn onto a spool to further reduce the filament diameter down to 200 μm. From there the same procedure

was followed with 45° offset layup, burnout, and final sintering. Therefore, the size study was able to achieve three unique brick sizes through the control of the filament diameter of either 500 µm, 300 µm, or 200 µm while still maintaining the same brick and mortar architecture. While the temperature study focused exclusively on the 200 µm structure made in accordance with *SP-45*.

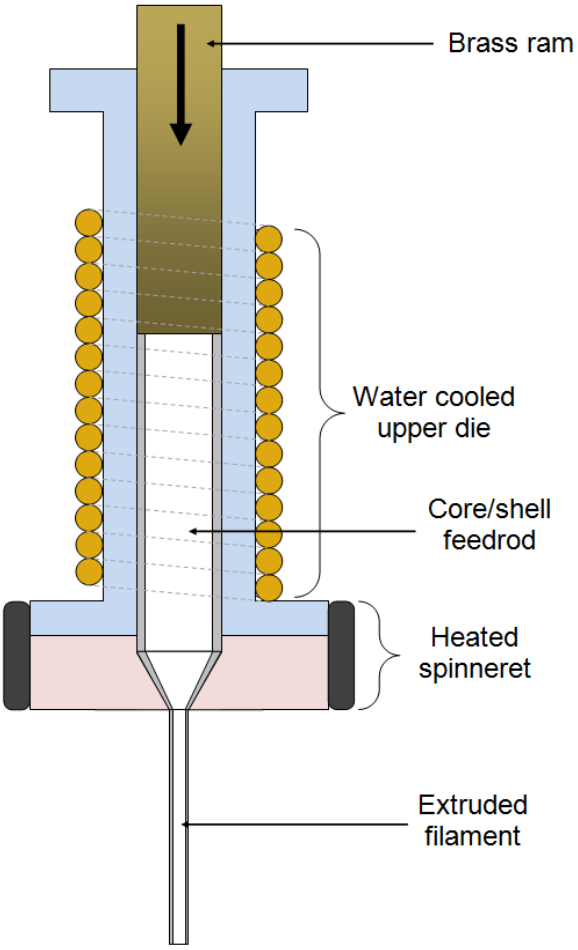


Figure 3.1: Schematic of the coextrusion assembly, showing how the core to shell ratio is maintained from a feed rod down to a filament.

Billets were pyrolyzed in an air furnace (10°C/h to 600°C, 2 h hold) to remove the EEA thermoplastic binder before sintering. The billets were then transferred to a BN-coated graphite hot-press die and placed inside a graphite hot press (Model HP20-3060, Thermal Technology Inc.) where they were heated to 1400°C at a rate of 15°C/min under flowing argon. Upon reaching temperature, a pressure of 32 MPa was applied to the die and held for 1 h after which the pressure was removed and the die was cooled to room temperature. An Al_2NiO_4 spinel would form along the Ni-Al_2O_3 interface that was reduced during a final heat treatment in flowing Ar-H_2 (5°C/min to 1000°C, 10 h hold) to reconstitute the nickel and alumina.

3.2. MICROSTRUCTURAL CHARACTERIZATION

To characterize the microstructure of the three series of ceramic-metal hybrids, samples were prepared for optical and scanning electron microscopy imaging. Specimens were mechanically polished using resin bonded diamond polishing pads down to a 1 μm diamond finish. Optical images were taken on a light microscope (Carl Zeiss Microscopy, model Lab.A1, Gottingen, Germany) for microstructural comparison. Images in the scanning electron microscope (SEM - Hitachi S-4300SE/N, Hitachi America, Pleasanton, CA, USA) were taken before and after failure in the three-point flexural tests using the secondary electron mode with a 20 keV accelerating voltage and a working distance of 12.2 mm.

Additionally, it was necessary to quantify the differences in the mortar interconnectivity as this is important to the brick-and-mortar nature of the material. Recently, contiguity has been used as a method to determine Al_2O_3/Ni interpenetration and connectivity [65]. Linear intercept analysis of microscope images was used to determine the number of brick/brick and brick/mortar interfaces and hence calculate the phase contiguity for Al_2O_3 and Ni, as described below. With this information and the known volume fraction of the two phases, phase separation and continuous volume can be calculated. **Tables 4.1** and **5.1** include measured values for the contiguity and calculated phase separation for nickel in the different structures. The single-pass coextrusion hybrids made by chopped/random and the 45° offset methods were the only ones to exhibit high values of phase separation, which correlates closely with the R-curve analysis.

3.2.1 Measurement of Microstructural Contiguity

The contiguity of a phase in a two-phase (α-β) mixture has been defined as the fraction of the total shared internal surface area between particles of the phase with particles of the same phase [66]:

$$C_\alpha = \frac{2S_V^{\alpha\alpha}}{2S_V^{\alpha\alpha} + S_V^{\alpha\beta}} \quad , \tag{1}$$

where C_α denotes the contiguity of the α phase, $S_V^{\alpha\alpha}$ is the interface area of the α particles per unit volume, and $S_V^{\alpha\beta}$ is the area of the interfaces between the α and β particles per unit volume. An approach to determine the contiguity of an α phase using simple intercept measurements on a micrograph of a random plane gives:[3]

$$C_\alpha = \frac{2N_L^{\alpha\alpha}}{2N_L^{\alpha\alpha} + N_L^{\alpha\beta}} \quad , \tag{2}$$

where $N_L^{\alpha\alpha}$ and $N_L^{\alpha\beta}$ are the random number of intercepts of the α/α and α/β interfaces within a random line of unit length on the examined planes. The separation of a phase, defined as the fraction of the total internal surface area of a phase that is shared between it and a separate phase, can be given as:

$$S_\alpha = \frac{2S_V^{\alpha\beta}}{2S_V^{\alpha\alpha} + S_V^{\alpha\beta}} = \frac{2N_L^{\alpha\beta}}{2N_L^{\alpha\alpha} + N_L^{\alpha\beta}} \quad , \tag{3}$$

where S_α is the separation of the α phase. Combining the above equations reduces the contiguity and separation for a single phase as equal to unity, i.e.,

$$C_\alpha + S_\alpha = 1 \, , \tag{4}$$

The same analysis can be performed for a β phase to yield another unity statement:

$$C_\beta + S_\beta = 1 \ , \tag{5}$$

where C_β and S_β are the contiguity and separation, respectively, of a β phase. The approach further proposes that for a given system, these identities are true if:

$$C_\alpha = S_\beta \quad , \tag{6}$$

$$C_\beta = S_\alpha \quad , \tag{7}$$

and thus, combining (4) or (5) with (7) or (6), respectively, will both yield the identity:

$$C_\alpha + C_\beta = 1 \quad , \tag{8}$$

This means that using a linear intercept analysis to determine the contiguity of the α phase will also yield the contiguity of the constituent β phase, i.e., in this study the contiguity of the nickel mortar. Finally, if the specific volume fractions of the α and β phases are known, then the contiguity terms can be used to determine the continuous volume:

$$f_{\alpha c} = f_\alpha C_\alpha \quad , \tag{9}$$

where f_α is the volume fraction of the α phase and $f_{\alpha c}$ is the continuous volume of the α phase [67].

3.3. MECHANICAL CHARACTERIZATION

To determine the mechanical behavior of the Al_2O_3/10Ni hybrid ceramics, beams were cut from the billets for flexural strength tests and for single edge-notched bend, SE(B), fracture toughness tests. All strength bars were cut to B-type specification (3 mm x 4 mm), in accordance with ASTM standard C1161 [68], and evaluated using a four-point flexure test. The tensile surface was aligned normal to the hot-pressing direction and polished to a 1-μm diamond finish. Beams were loaded on an Instron 5881 electro-mechanical testing machine (Instron Corp., Norwood MA, USA) at a crosshead speed of 0.1 mm/min with upper and lower loading spans of 20 and 40 mm, respectively. Strain was directly measured using a linear variable differential transformer (LVDT) in contact with the tensile surface of the bars. Five (N = 5) bars for each

sample series were tested for average strength properties, while four (N = 4) SE(B) bars were split between initiation toughness and R-curve analysis depending on their fracture behavior.

An open air furnace attachment for the Instron 5881 was used for the elevated temperature strength tests. Temperatures of 600°C, 700°C, 800°C, and 900°C were chosen using the fact that the yielding of nickel would be severe beyond 2/3 its absolute melting temperature. T_m of nickel is 1455°C and that gives an upper limit ($2/3*T_m$) of 879°C using the Kelvin conversion for the absolute scale. For the strength tests a fully articulating SiC four-point fixture was used in accordance with ASTM standard C1161 for B type specimens. Samples were heated at 10°C/min to the testing temperature, allowed to equilibrate for 10 minutes at temperature and were then tested at 0.1 mm/min crosshead speed with a high temperature LVDT to directly measure strain.

Fracture toughness tests on the SE(B) specimens were performed in three-point bending to determine the crack-initiation fracture toughness K_{Ic} of the hybrid ceramics, using linear-elastic fracture mechanics in accordance with ASTM standard E1820 [69]. Each beam was cut to a length of ~25 mm, with a cross-sectional width W = 4 mm and thickness B = 4 mm. A straight notch of 1.8 mm was cut into the tensile surface of the sample using a low speed saw with a wafering blade. The notch root was subsequently sharpened using a micro-notching technique involving polishing the root with a razor blade immersed in 3-µm diamond solution under a constant load. This allowed for a final notch root radius below 30 µm and a crack length, a, to width ratio, a/W, of ~0.5. The bars were polished down to a 1-µm surface finish to minimize the effects of surface flaws during the loading of the beams. Three-point bend tests were performed with a load span of 16 mm on a screw-driven Instron 5944 testing machine.

Based on the results of these crack-initiation K_{Ic} toughness tests, full nonlinear-elastic fracture mechanics J-based crack-resistance curves, $J_R(\Delta a)$-curves, were determined for those samples that exhibited nonlinear load-displacement behavior in an attempt to capture both the elastic and plastic contributions to deformation and crack growth, in general accordance with ASTM standard E1820 [69]. Additional 4 mm x 4 mm bars were polished and razor notched and tested *in situ* in the Hitachi S-4300SE/N SEM using a Deben MicroTest 2 kN (Deben, UK) bending stage. This setup allows for quantitative measurement of the crack extension (Δa) and the crack-growth toughness in terms of the resistance-curve (R-curve) behavior, with simultaneous real-time observation of the interaction of the crack path with the salient features of the microstructure. Samples were tested to a maximum crack extension Δa_{max} capacity of 550 µm, specified by ASTM E1820 for plane-strain J_{Ic} fracture toughness measurement, where $\Delta a_{max} = 0.25 b_0$ (b_0 is the initial uncracked ligament). To quote toughness in terms of the stress intensity, K, the standard mode-I J-K equivalence, $K_J = (J\,E')^{1/2}$, was used to convert values of J_{Ic} to K_{JIc}, where $E' = E$ (Young's modulus) in plane stress and $E/(1-\nu^2)$ in plane strain (ν is Poisson's ratio). Values of E were determined via impulse excitation and calculated with a modified long bar approximation using ASTM C1259 [70], with ν, the Poisson's ratio for alumina, taken to be ~ 0.23.

For elevated temperature R-curve analysis, a different method was necessary, as the *in situ* SEM stage was incapable of anything outside of room temperature. Therefore, compliance evolution during cyclic loading was used to determine the crack length. Compliance can be determined experimentally using the equivalence found in ASTM E1820 of:

$$C = \frac{\Delta\delta}{\Delta P} \quad , \tag{10}$$

where $\Delta\delta$ and ΔP are the change in displacement and change in load, respectively, of the linear elastic portion of the loading cycle before each failure event. This can then be used to determine the crack length:

$$a_n = a_{n-1} + \frac{W - a_{n-1}}{2}\frac{C_n - C_{n-1}}{C_n} \quad , \tag{11}$$

where W is the measured thickness and C and a are the compliance and crack length determined at the intervals n or n-1. From there the calculations follow ASTM E1820 identically as described earlier for the room temperature *R*-curves. Therefore, 4 mm x 4 mm bars were polished and razor notched before being inserted into a three-point SiC fixture for the open air furnace on the Instron 5881. Specimens were heated at 5°C/min to avoid thermal shocking the notched sample and were allowed to equilibrate at temperature for 10 minutes before testing commenced at a crosshead rate of 0.05 mm/min with an LVDT in contact with the bottom of the bar. Samples were loaded until failure commenced and then immediately unloaded and reloaded cyclically, allowing for the determination of the compliance each time the crack propagated. It should be noted that there is the potential for microcracking to occur during this unloading cycle, which would lead to increased crack length and hence, artificially lower *R*-curve values. This could then be considered a more conservative method, which I believe is appropriate for this indirect method of measuring crack length without the crack mouth opening displacement.

Chapter 4
Optimization of Brick Morphology

4.1. RESULTS and DISCUSSION

4.1.1. Microstructure

Extrusion parameters, such as rheology of the plastic/powder suspension and velocity, can lead to significant microstructural differences between the various hybrid structures. Post extrusion parameters such as filament length and laminate thickness can change the aspect ratio of the individual bricks of ceramic material. Varying these parameters is necessary to tune the hybrid architecture to the desired structure and hence to the ideal properties for the ceramic/metal composition. This is necessary, in part, due to the coarseness of the structure that is produced. While coextrusion allows for precision control of the metallic content of these structures, it produces bricks that are around an order of magnitude larger than their nacre counterparts as well as having a reduced aspect ratio in comparison. Varying these parameters allows for some degree of manipulation to control the size and shape of the bricks to a certain degree.

These six Al_2O_3/10Ni microstructures (**Figure 4.1**) all had ~90 vol.% ceramic content, controlled by manipulating the shell thickness on the initially fabricated feed rods of Al_2O_3/NiO thermoplastic suspensions. Differences in solids loading of each thermoplastic, and the volume reduction of the NiO after it was reduced to Ni, was accounted for in calculations of the cross-sectional area of each material. To quantify these structures, image analysis was performed on cross-sections using ImageJ [71], with results summarized in **Table 4.1**; notably, the average Ni-boundary thickness and width/thickness of the bricks were measured. For the *SP-chop* and *SP-45* structures, which were relatively constrained during lamination, the bricks were over twice as wide as they were thick, with an average mortar thickness of ~12.5 µm. With the *SP-lam* structures which were processed with unconstrained lamination, this aspect ratio increased three-fold, with brick widths some six times their thickness. Additionally, the average mortar thickness was reduced to ~10 µm, with a significant reduction in the mortar contiguity, which dropped from ~0.9 to 0.5; this lowers the mortar interconnectivity, i.e., a larger portion of alumina bricks are in direct contact instead of being separated by nickel.

The multipass structures exhibited certain similarities to the *SP* structures. *MP-chop* and *MP-45* structures had brick aspect ratios (~2.5) and mortar thicknesses similar to their *SP* counterparts, whereas *MP-lam* structures showed a threefold increase in aspect ratio to 6.3 and a reduced mortar thickness (compared to *MP-chop* and *MP-45*), mirroring results for single-pass extrusions. However, unlike *SP* structures, the *MP* series all displayed much lower Ni-boundary interconnectivity and matrix contiguity, suggesting that additional manipulation of the extruded filament caused the NiO "shell" to deform in a detrimental manner, through unconstrained lamination of the filament in the *SP* series or secondary extrusion in the *MP* series.

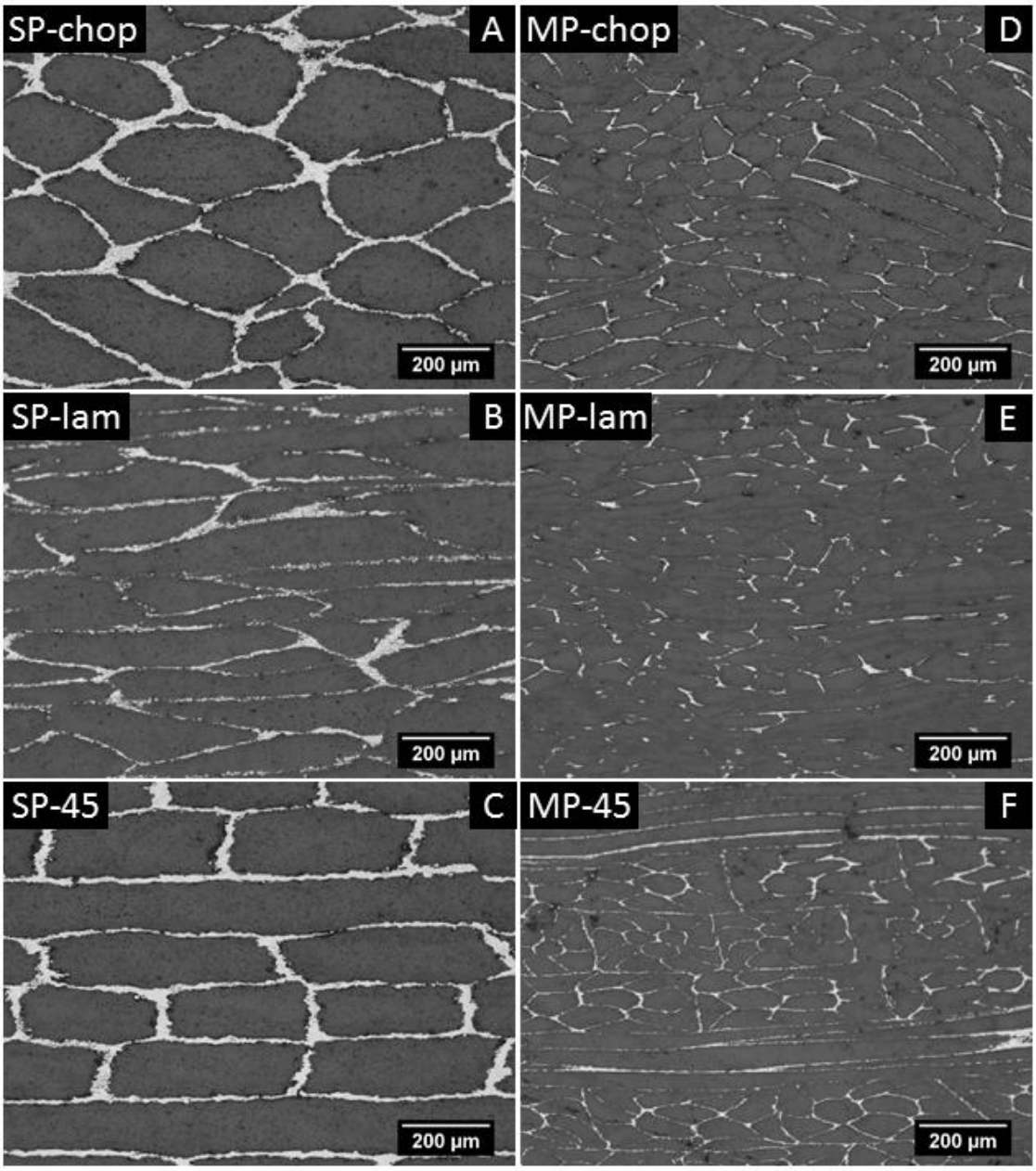


Figure 4.1: Optical micrographs of the resulting Al_2O_3/10Ni metal compliant-phase ceramics: (**A-C**) single-pass coextrusions to 300 µm, specifically the *Sp-chop* structure (chopped and laminated in constrained die), *SP-lam* (chopped and pre-laminated into sheets), and *SP-45* (oriented filament laminated into sheets and consecutively offset 45° from the previous layer); (**D-F**) multipass coextrusions counterparts *MP-chop*, *MP-lam* and *MP-45*, that were extruded to 6 mm, then bound together and extruded again to 300 µm. The brighter phases are nickel metal while darker phases are the alumina ceramic. Details of the procedures used for microstructural characterization are given in section 3.2 of the previous chapter.

Table 4.1. Microstructural information for the six Ni compliant-phase ceramic structures, shown in **Figure 4.1** and developed by single and multipass coextrusion in this study.

Structure	Ni Contiguity* (C_{Ni})	Continuous Volume Ni (f_{NiC})**	Mortar Thickness (μm)	Brick Thickness (μm)	Brick Width (μm)	Width/ Thickness	Elastic Modulus (GPa)
SP-chop	0.875	8.92%	12.6±4.4	135.9±30.8	329.3±70.8	2.42	182±7
SP-lam	0.471	4.80%	10.1±2.9	79.7±18.9	506.9±138.4	6.36	217±22
SP-45	0.899	9.17%	13.6±5.8	124.6±11.3	308.4±27.1	2.47	238±17
MP-chop	0.279	2.85%	7.7±1.6	34.2±8.0	93.1±35.0	2.72	208±11
MP-lam	0.146	1.49%	5.5±1.32	26.1±6.0	165.4±54.1	6.34	224±13
MP-45	0.249	2.54%	8.2±1.5	44.1±8.2	89.7±19.2	2.03	214±11

* details of how microstructural contiguity was quantified is given in Chapter 3.2.
**possible maximum is 10.2%.

4.1.2. Strength Properties

Four-point bending tests were performed to determine their flexural strengths of these structures (**Figure 4.2**). Average strength levels are significantly lower than that of the Al_2O_3 standard. This trend is expected when adding a secondary phase with a lower strength, but notably this strength difference falls closer to the expected lower-bound (258 MPa), rather than upper-bound (437 MPa), strength from a "rule of mixtures" calculation. Likely causes are that the hybrid ceramics display a coarse-grained structure, with brick sizes much larger than the ~5-μm alumina grain size, a continuous boundary of weaker nickel can result in a composite strength that is more associated with that of nickel, and a weak ceramic-metal interface can translate throughout the structure along the continuous Al_2O_3/Ni contact area. Indeed, the strengths of the single and multipass structures were roughly constant (~200 MPa), the one exception being the *SP-chop* structure which had a strength of 120 MPa, likely resulting from its very low Ni-mortar contiguity and brick aspect ratio. Additionally, values for the elastic modulus for each series can be found in **Table 4.1**, which follow a similar trend to the strength values. The series with low contiguity have modulus values that fall within a standard deviation of each other, while the high contiguity series, *SP-chop* and *SP-45*, have distinctly lower and higher values respectively. All of these structures have values that fall closer to the lower bound rule of mixtures for the elastic modulus (261 GPa) with *SP-45* being the highest in part due to its microstructural similarities to the composite models for the upper bound modulus which assume continuous unidirectional fibers., *SP-45* has continuous bricks that extend throughout the bulk of the structure, though only unidirectional in each respective layer.

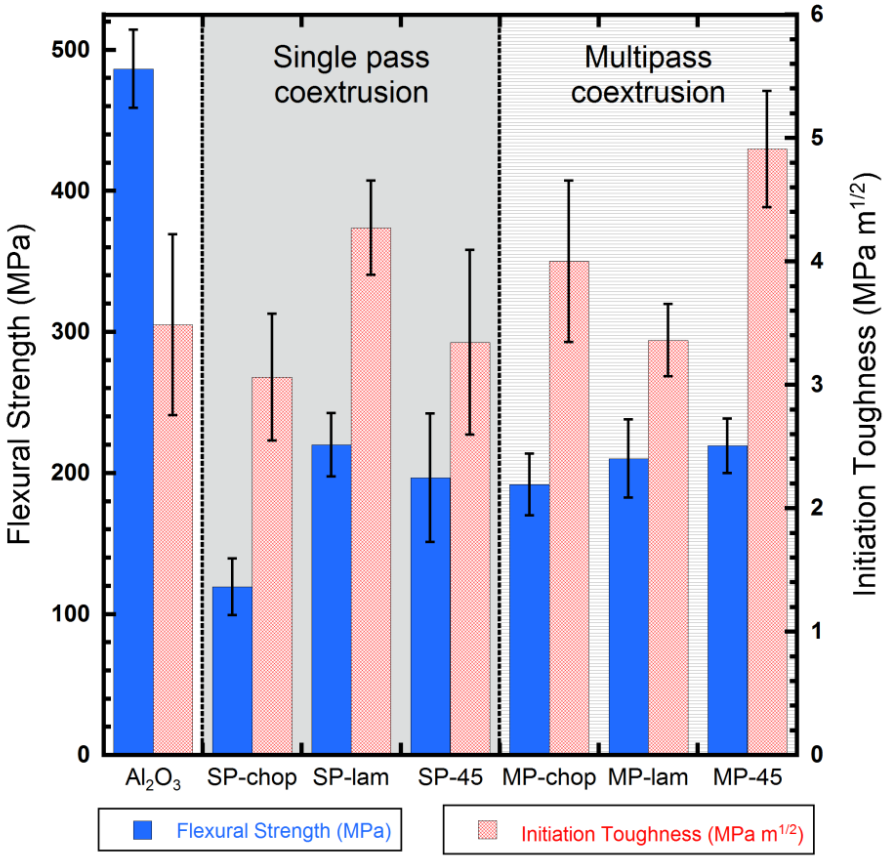


Figure 4.2: Four-point bending data of the strength and initiation toughness of the six Al_2O_3/10Ni compliant-phase ceramic microstructures, as compared to that for the comparable monolithic Al_2O_3 standard. All the alumina structures containing the Ni compliant phase had a markedly lower strength, but were within 20-30 MPa of each other, the exception being the single-pass coextrusion material that was subjected to constrained lamination.

4.1.3. Fracture Toughness Properties

To characterize resistance to failure, fracture-toughness tests were first performed on the hybrid ceramics in three-point bending; results are given in **Figure 4.2** with the strength values. All coextruded structures had crack-initiation fracture toughness values that were relatively close to pure alumina, i.e., ~3 to 5 MPa.m$^{0.5}$. The *SP-lam* and all *MP* structures exhibited catastrophic fracture during loading with no sign of deviation from a linear crack path (**Figure 4.3**), similar to the Al_2O_3 standard. For monolithic alumina, this can be associated with its small grain size, since the most significant *R*-curve behavior is seen in alumina ceramics with larger (≥25 μm) elongated grains where intergranular cracking ensues to promote interlocking grain bridging. Such crack-bridging is also impeded in the *SP-lam* and *MP* series, owing to their low mortar contiguity, allowing fracture to take place unimpeded from brick to brick.

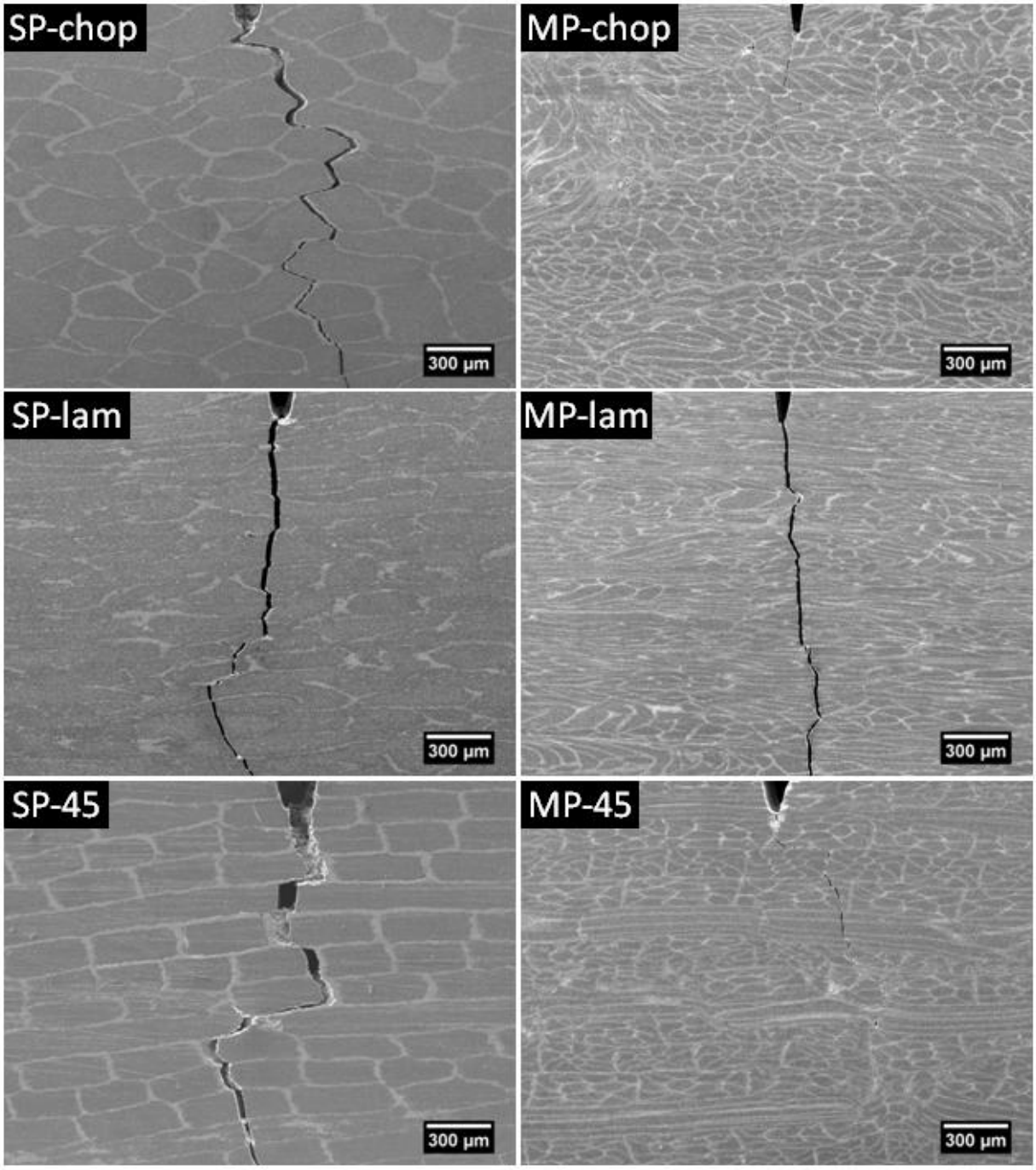


Figure 4.3: SEM micrographs showing the crack paths for all Al_2O_3/10Ni compliant-phase ceramic microstructures, post-failure from the notched toughness flexural test. Note that significant crack deflection can be seen in the *SP-chop* and *SP-45* samples (*SP-45* shows additional elastic bridging and some grain pull-out). These represent structures from the single-pass coextrusion while all the multipass structures (*MP* series) have relatively straight-through cracks with little to no evidence that the Ni mortar had any effect on the nature of the composite failure.

In contrast, the *SP-chop* and *SP-45* structures exhibited non-catastrophic failure, specifically involving stable (subcritical) cracking with significant deflections along the path of the

propagating crack. This is especially evident in the *SP-45* structure (**Figure 4.4**) where a crack can be seen to advance primarily around the bricks through the Ni mortar interphase regions to create a more tortuous crack path with evidence of both crack deflection and grain bridging with limited grain pull-out. From the perspective of extrinsic toughening, this represents a desirable crack path, and accordingly *R*-curve analysis was performed on both the *SP-chop* and *SP-45* series to further evaluate their toughness. Similar to the *SP-lam* and all *MP* structures, no *R*-curve could be measured for the *SP-chop* samples as they simply failed catastrophically on crack initiation. However, the load-deflection behavior for the *SP-45* series showed extensive subcritical cracking over millimeter-sized crack extensions, resulting in marked rising *R*-curves (**Figure 4.5**). Of all the coextruded metal/ceramic hybrids examined, this structure most resembled the brick-and-mortar architecture of natural nacre and clearly was the toughest.

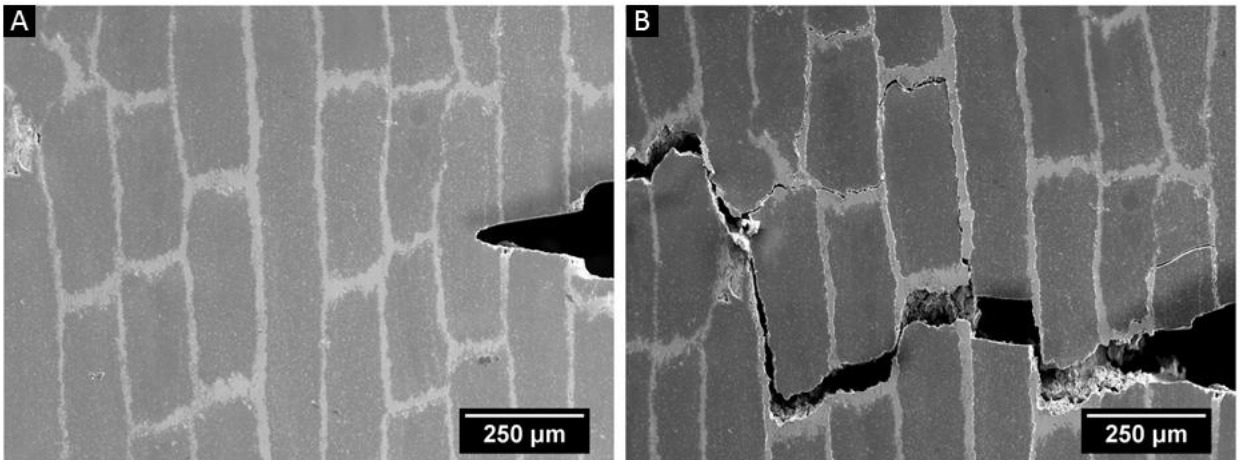


Figure 4.4: (**A**) is before loading had begun with a clearly visible razor micronotch and (**B**) is after failure had occurred. Multiple crack paths can be seen deflecting around the individual bricks leading to crack bridging and brick pull-out, with failure occurring primarily along Al_2O_3/Ni boundaries, and brick failure within the inter layers that are oriented normal to the micro-notch.

The crack-growth resistance curves provide valuable insight into the nature of these materials in generating toughness from their capacity to sustain subcritical (non-catastrophic) crack growth through their microstructures. As noted, the crack-initiation toughness of the *SP-45* structure was low, characteristic of virtually all hybrid ceramics, and measured to be ~2-4 MPa.m$^{0.5}$, which is comparable to that of pure alumina (~3-4 MPa.m$^{0.5}$). However, the effect of extrinsic toughening with crack growth, over crack extensions of Δa ~ 500 to 1000 µm or more, resulted in the *SP-45* hybrid structure displaying a toughness as high as ~12 MPa.m$^{0.5}$. This is to be compared with that of coarse (25 µm grain size) monolithic alumina which displays a shallow *R*-curve rising up to ~4 MPa.m$^{0.5}$; this material failed intergranularly with subcritical cracking stabilized by crack deflection and limited grain bridging. With the Al_2O_3/Ni complaint-phase *SP-45* ceramic, the comparable "grains" are now the alumina bricks; as these are significantly larger bricks (>200 µm) in the coextruded brick-and-mortar structure, they are able to more effectively bridge the crack and locally arrest it. *R*-curve slopes are correspondingly far steeper than in monolithic alumina, with a roughly two-fold increase in toughness over 500 to 1000 µm of crack extension, indicative of significant near-tip extrinsic toughening. Indeed, despite having a much higher ceramic content, the best Al_2O_3/10Ni compliant-phase ceramic hybrid (*SP-45*) displays a higher toughness and steeper *R*-curve than that of a cellular Al_2O_3-20 vol.% Ni composite (measured

with double cantilever beam samples in ref. [72]). Additionally, the *SP-45* ceramic also displays *R*-curve behavior similar to SiC/PMMA (polymethyl methacrylate) brick-and-mortar composites made via freeze casting. These SiC/PMMA composites had a finer brick structure (~10 μm thick) and significantly lower ceramic content (40-60 vol%) with a polymeric mortar which exhibited expected plastic behavior during failure unlike the Al_2O_3/10Ni ceramics.

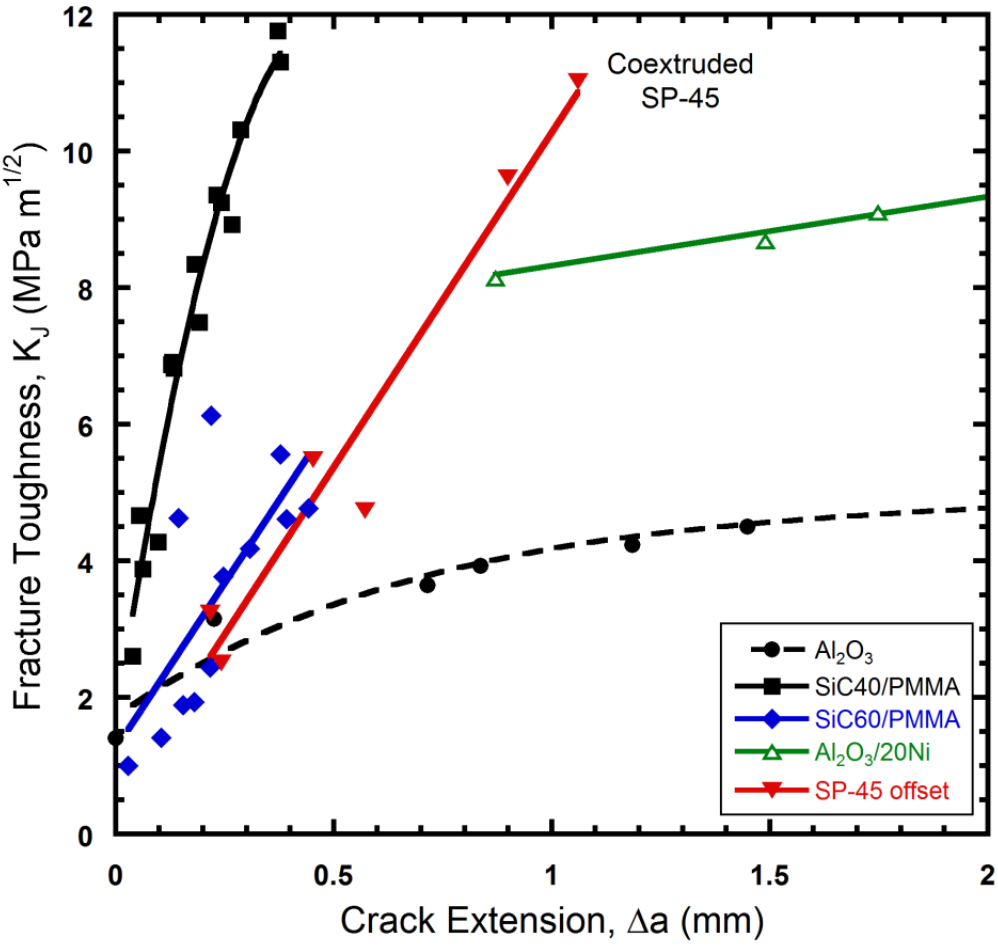


Figure 4.5: Fracture-toughness R-curves, in terms of the stress intensity, K_J, back-calculated from nonlinear-elastic *J*-measurements (details given in the online Supplementary Information), comparing the *SP-45* offset structure with monolithic 25-μm grain-sized alumina [73] and freeze-cast SiC-PMMA brick-and-mortar composites [8]. Results are also compared with a cellular Al_2O_3/20vol.%Ni composite [72], tested using double cantilever-beam specimens which allow for pronounced crack extensions due to their larger specimen widths. Our coextruded Al_2O_3/10Ni *SP-45* structure, however, can be seen display far superior *R*-curve toughness.

In situ SEM measurements of the *R*-curves reveal a range of extrinsic toughening mechanisms in the *SP-45* structure, notably the crack tends to follow the "mortar" regions, which gives rise to crack deflection and ceramic "brick" pull-out, both of which contribute to the *R*-curve (crack-growth) toughness of the Al_2O_3/10Ni composite (**Figure 4.5**). However, the displacements in the Ni mortar appear to involve interface failure of the Al_2O_3/Ni boundaries, rather than deformation within the Ni mortar itself, which means that in terms of

strength/toughness properties the full potential of these composites has yet to be realized as best properties are predicted [36] to be achieved by utilizing a mortar with high tensile and shear resistance (the mortar strength must not, however, exceed that of the ceramic, or else the ceramic "bricks" will simply fracture with the result that the ductility and toughness will be lost). However, these compliant-phase ceramics still have some high temperature potential, as higher temperatures will increase the ductility of the mortar phase, meaning the interfacial strength might be sufficient to allow mortar deformation at elevated temperatures.

Contiguity of the nickel boundary can also be seen to play a significant role in the toughening behavior of these materials. Comparing the contiguity and continuous Ni volume data from **Table 4.1** with the crack path images in **Figure 4.3** shows an interesting correlation of these measures of mortar interconnectivity with the cracking behavior. The two structures with high mortar contiguity are the previously mentioned *SP-chop* and *SP-45* series. These two structures show many of the premier brick-and-mortar behaviors such as elastic bridging and brick pull-out, while all the other structures have primarily straight through-cracks with relatively low contiguity values. This suggests that high interconnectivity of the mortar phase in brick-and-mortar structures can be a method to predict whether or not a composite will exhibit failure in a similar fashion to natural brick-and-mortar structures. The challenge of producing low volume fraction mortar is now coupled with the challenge of guaranteeing that the mortar is also well dispersed through the composite.

While models [35-41] have predicted the crack deflection, crack bridging, pull-out and mortar deformation behavior of specific brick/mortar combinations, few "nacre-like" compliant-phase ceramics have ever been produced that have a high ceramic volume fraction, approaching that of aragonite in natural nacre, and a continuous metallic mortar, which is predicted to confer improved damage-tolerant properties compared to polymer mortars. As such high ceramic volume fraction brick-and-mortar structures with a metallic compliant phase are extremely complex to make with freeze-casting, the coextruded structures developed here permit mechanistic observations in these nacre-like ceramics, and in many ways represent an ideal biomimetic architecture, apart from the fact that the structures are coarse and the ceramic/metal interfaces are weak, both factors that limit the strength of these materials. The model structures developed using coextrusion in the present study permit mechanistic observations of failure in these bioinspired nacre-like ceramic materials, and in many ways represent an ideal biomimetic architecture, apart from the fact that the structures are too coarse and the ceramic/metal interfaces are weak, both factors that limit the strength of these materials. As the data in **Figure 4.2** show, a notable drop in strength occurs in the ceramic structures with the addition of the low strength metal phase, which is primarily associated with this highly coarse nature of the hybrid microstructures and easy failure along the Al_2O_3/Ni boundaries. This strength reduction is close to the theoretical lower-bound rule of mixtures between alumina and nickel, and is the expected result of including a continuous nickel phase instead of interdispersed grains. A continuous or semi-continuous mortar phase significantly increases the amount of alumina/nickel boundary area within the composite, and if this boundary region is particularly weak then it can dictate the final properties to a significant degree. In this case, the cracking behavior along the alumina/nickel boundary seen in **Figures 4.3** and **4.4** suggest that this is the apparent case for these composites. Future development will need to focus on the interfacial properties of these ceramic and metal systems, as a weak interface will lead to the interfacial delamination seen in

Figure 4.4, while too strong of an interface will result in fracture of the ceramic bricks and a corresponding loss in toughness.

4.2. SUMMARY

Coextrusion can be considered a viable route to synthesizing bioinspired "brick-and-mortar" architectures, as the process can be manipulated to form different microstructures with optimized properties and further can achieve high ceramic contents of ~90 vol.%, akin to nacre, with metallic mortars; such structures are essentially impossible to make with freeze-casting. Additionally, coextrusion can further improve upon the content of the hard ceramic phase (>95 vol.%) simply by reducing the feedrod shell thickness, with the only limitation being that the particle size stay below the final mortar thickness.

The mechanical properties of our compliant-phase ceramics were either comparable or superior to traditional ceramic-metal composites. Flexural strengths were not high due to the coarse microstructures, consistent with a similar trend seen in traditional coextruded fibrous monoliths [61]. However, our *SP-45* brick-and-mortar architecture displayed extensive *R*-curve toughening with a three-fold toughness increase compared to the crack-initiation value due to stable cracking, with the interconnectivity of the Ni mortar playing a critical role in dictating crack paths. Toughening was largely associated with crack deflection along the weak Al_2O_3-Ni interfaces; although negating the beneficial role of the metallic mortar, this nevertheless provided for some sliding displacements between the ceramic bricks, resulting in crack bridging and brick pull-out, which is vital to inducing *R*-curve toughening to stabilize subcritical crack growth, thereby mirroring behavior in natural nacre.

Improved damage-tolerant properties should be further achieved through the development of finer structures, and by strengthening the ceramic/metal interfaces, so that inter-brick displacements can occur within the metallic mortar phase; both factors predicted [36] to enhance both strength and toughness. This can be achieved through extrusion or drawing smaller diameter filament to reduce the brick size, or through the inclusion of an intermediate feedrod layer between the Ni and Al_2O_3 that bonds strongly to both materials, discouraging interface failure. Filament drawing from the extruder hallows for further reduction of a single extrusion past the 300 μm limit, and it is not aggressive at reducing the brick size as the multipass extrusion, which should allow for smaller brick size without the detrimental effects to the mortar contiguity. Further interface strengthening can be achieved through reactive hotpressing of a coextruded system of Al-NiO, which has been shown to create interpentrating Al_2O_3-Ni composites with evidence of ductile deformation [74]. The authors are currently attempting several of these methods to improve the damage tolerance of the existing structures. As such we believe that coextrusion opens the door to a new range of possibilities of engineering and design with flexible ceramic manipulation, complex 2D cross sections, and advanced interface architectures [57].

Chapter 5
Observations of Size Effects on Mechanical Behavior

5.1. RESULTS

5.1.1. Microstructure

As noted in the previous chapter, the process of coextrusion can be modified readily to change the brick morphology simply by varying the extruded filament diameter. By leaving the ceramic content and mortar-to-brick ratio constant, I produced a series of microstructures that varied only in brick size while maintaining the same architecture as *SP-45* previously shown.

Figure 5.1 shows examples of three well-formed (nacre-like) brick-and-mortar structures comprising a high-volume fraction (~90 vol.%) of alumina bricks with a metallic nickel mortar in between. The microstructural images are representative of any cut made normal to the hot pressing direction, as the 45° layer offset helps produce a radial symmetry akin to the platelet structure in nacre. These were made with the same ~10 vol.% nickel mortar phase using three filament diameters, specifically (A) 500 µm, (B) 300 µm and (C) 200 µm, which represent the nominal brick widths. The structures were batched and processed identically, with the intent to vary only the brick size and mortar thickness. The images also indicate a well-sintered microstructure with little to no obvious porosity.

While the structures varied in brick size and mortar thickness, it is important to note that mortar interconnectivity and brick aspect ratio were not affected detrimentally during the processing. Microstructural data, listed in **Table 5.1**, indicate the aspect ratios of the Al_2O_3 bricks, their size and the mortar thickness. While the average brick size is reduced by 35% between 500 and 300 µm series, and 41% between the 300 and 200 µm series, the aspect ratios vary only slightly (2.35 - 2.51). The mortar thickness follows a similar downward trend from 17.9 µm to 11.7 µm to 6.9 µm, which is expected with the reduced filament thickness. Additionally, in the previous chapter it was noted that a high contiguity, and therefore a high matrix interconnectivity, of the matrix phase trended positively with the overall mechanical behavior of the resulting hybrid structure. The measured contiguity of the three structures also shows little to no variation (0.886 - 0.938) which was well within the acceptable range seen in the previous study. Hence, these structures were expected to less likely result in the fracture of bricks, but rather to induce crack deflection along the brick/mortar interfaces or preferably within the mortar itself.

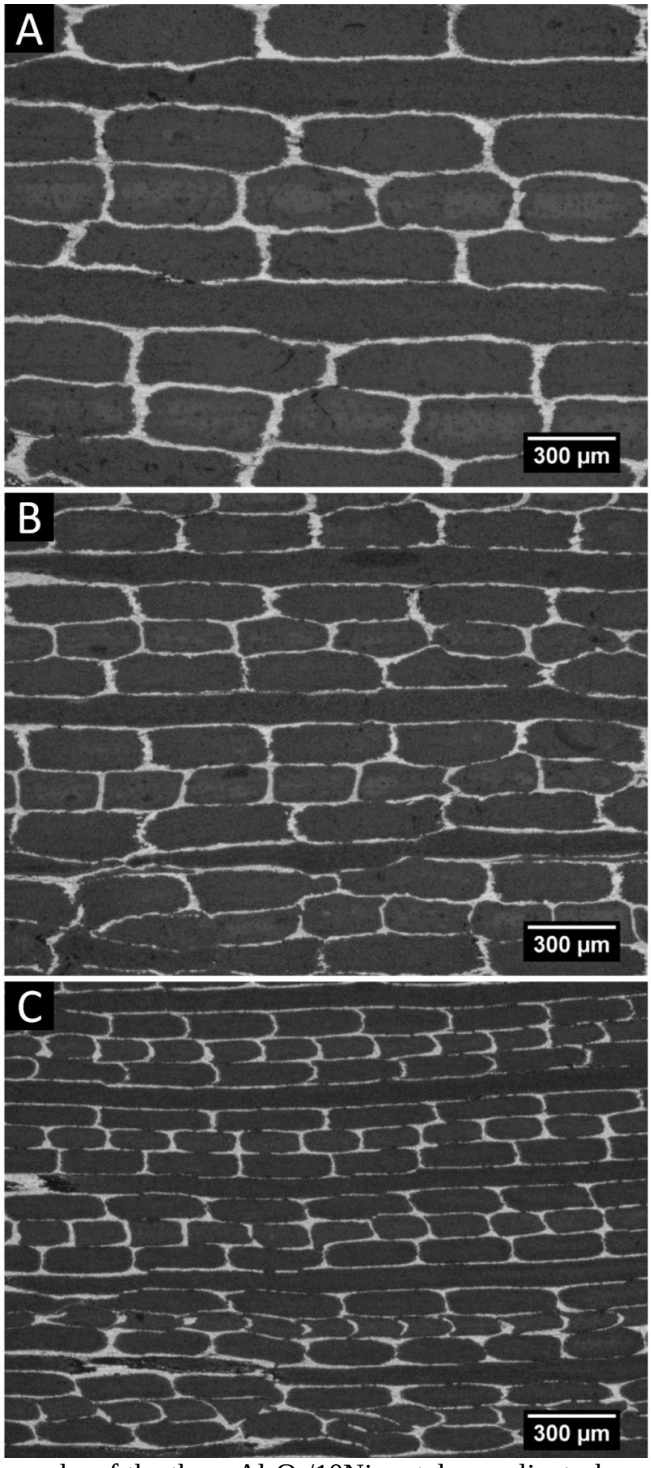


Figure 5.1: Optical micrographs of the three Al_2O_3/10Ni metal compliant-phase ceramics made with: (**A**) 500 µm filament, (**B**) 300 µm filament, and (**C**) 200 µm filament produced through coextrusion.

Table 5.1: Microstructural information for the three Ni compliant-phase ceramic structures, shown in **Figure 5.1** and developed by coextrusion of different filament diameters.

Structure	Ni Contiguity (C_{Ni})	Continuous Volume Ni (f_{NiC})*	Mortar Thickness (μm)	Brick Thickness (μm)	Brick Width (μm)	Width/ Thickness	Elastic Modulus (GPa)
200 μm	0.886	9.03%	6.9±1.4	74.2±7.0	186.4±12.8	2.51	318
300 μm	0.894	9.11%	11.7±3.9	125.3±15.0	292.9±23.0	2.34	215
500 μm	0.938	9.56%	17.9±3.8	182.2±15.6	430.7±18.1	2.36	227

*possible maximum is 10.2%

5.1.2. Mechanical Characterization – Strength and Toughness

Four-point bend tests were performed to determine the flexural strength of the three unique microstructures; results are shown by the blue columns in the histogram in **Figure 5.2**. As the brick size decreases we see strength trend upwards from 110 ± 8 MPa for the 500 μm structure up to 158 ± MPa for the 200 μm structure with the 300 μm structure in between the two at 113 ± 18 MPa. Although these flexural strengths show a ~45% increase with a 60% decrease in brick size, these values are lower than the strength of pure alumina (~400 MPa), results which are not unexpected as similar numbers were found the morphology study of these coextruded alumina/Ni hybrid ceramics.

Corresponding evaluation of the toughness of these ceramic-Ni hybrids was made initially on linear-elastic fracture mechanics tests in micro-notched three-point bending to measure K_{Ic} values; such crack-initiation values are shown by the pink columns in the histogram in **Figure 5.2**. Akin to the flexural strengths, the toughness of the brick-and-mortar structures strongly correlates with reduced brick size. Specifically, K_{Ic} values increase just over 20%, from 3.4 MPa.m$^{1/2}$ to 4.1 MPa.m$^{1/2}$, with a 60% reduction in brick size from nominally 500 μm to 200 μm, respectively.

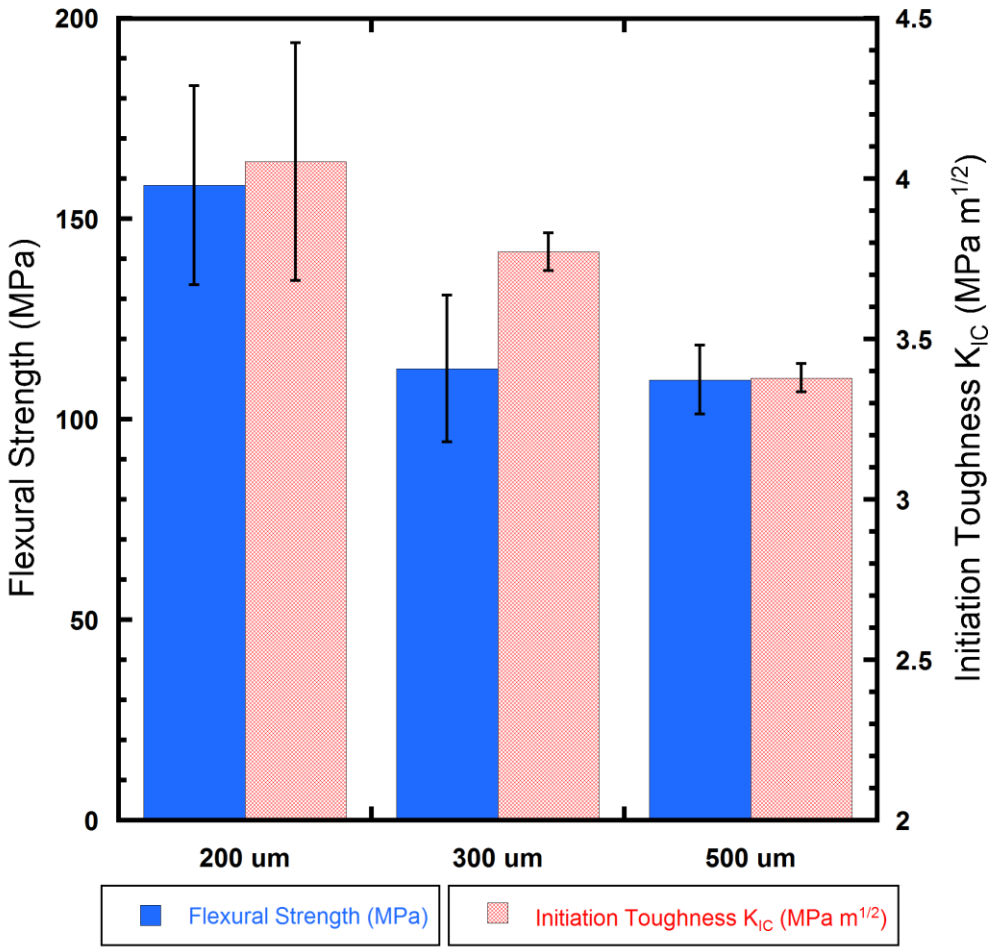


Figure 5.2: Four-point flexural strength for the three microstructures shows a ~45% increase with a 60% decrease in brick size from 500 to 200 μm. Corresponding crack-initiation K_{Ic} fracture toughness values increase by just over 20% for the same decrease in brick size, indicating an improved overall mechanical performance as the brick-and-mortar structure is refined.

However, as the principal contributions to toughness in such brick-and-mortar ceramics are achieved extrinsically during crack growth, additional nonlinear-elastic J_R-curve measurements were performed to measure resistance-curve behavior as a basis of evaluating the crack-growth toughness of these structures. Resulting R-curves, generated by *in situ* testing in three-point bending in the SEM with real time observations of crack growth, are shown in **Figure 5.3**, and are expressed in terms of stress-intensity K_J values. As was mentioned earlier, the maximum valid K_J value that can be obtained from R-curve analysis is given at $\Delta a_{max} = 0.25 b_0$, which is ~550 μm in the case of these specimens. All three structures showed marked rising R-curve behavior with the crack-growth toughness being inversely related to the fineness of the microstructures. Defined in terms of the slope of the R-curves, strictly "valid" crack-growth toughness values varied from 6.6 MPa.m$^{1/2}$ in the 500-μm brick sized structures to 12.6 MPa.m$^{1/2}$ in the 200 μm structures, a 92.6% increase in toughness for a 60% decrease in brick size. Although monolithic alumina tends to fracture catastrophically, all three nacre-like structures were able to sustain stable crack extensions in excess of Δa ~ 1 mm, with toughness values well

in excess of 15 MPa.m$^{1/2}$, *i.e.*, at least a factor of two greater than any reported toughness values for monolithic alumina (**Figure 5.3**).

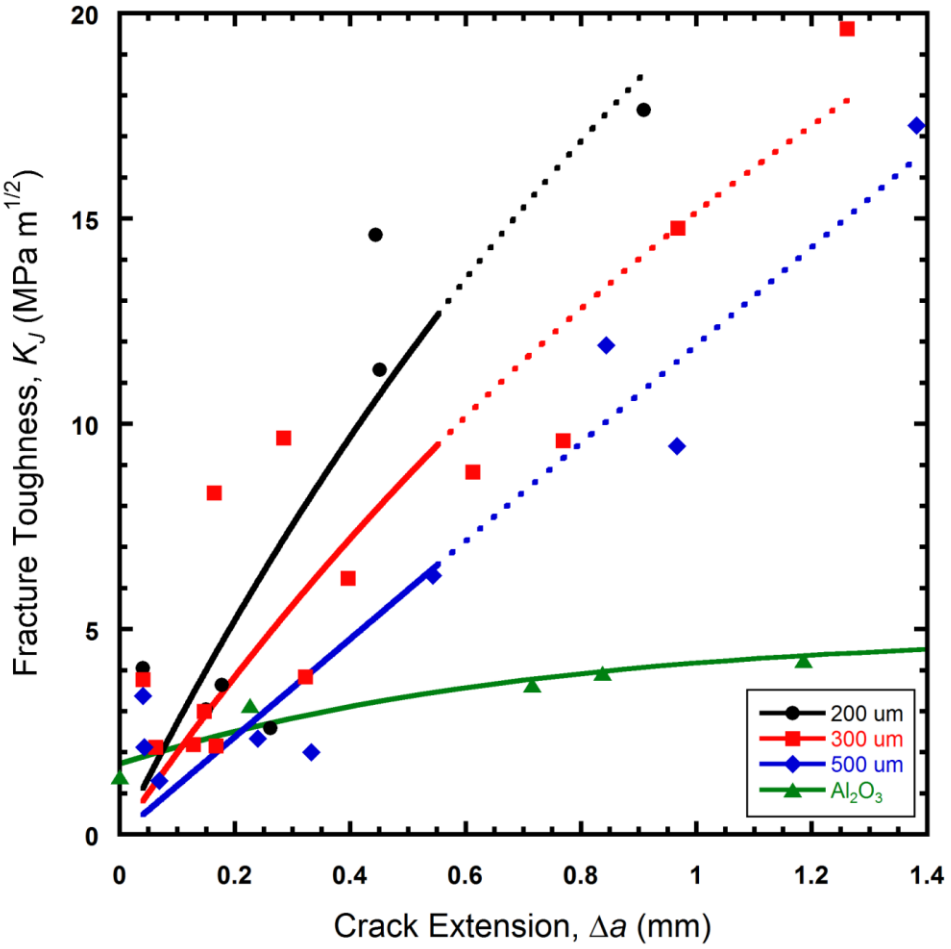


Figure 5.3: Crack-growth resistance curves measured using *in situ* three-point bend tests in the SEM. Results were obtained using nonlinear elastic fracture mechanics in terms of *J*, which were then converted into stress intensity K_J values (see Chapter 3). All three structures, with brick sizes varying between 200 and 500 μm, can be seen to exhibit rising R-curve behavior with K_J values exceeding 15 MPa.m$^{1/2}$; there is further a clear trend of steeper curves with decreasing brick size. Compared against these three structures is that of pure Al_2O_3 [73] which has a very shallow, almost flat R-curve.

5.1.3. Crack-Growth Observations

Corresponding observations of the crack paths during the *in situ* measurements of *R*-curves in the SEM are shown in **Figure 5.4**. While cracks were observed to pass through the bricks on occasion, the majority of the crack advance was primarily to follow the mortar phase; this can lead to significant crack deflection away from the plane of maximum stress, particularly for the 200 and 300 μm brick-sized microstructures. The existence of mortar layers perpendicular to the growing crack were also seen to cause crack bifurcation, leading to increased microcracking (**Figure 5.4**). This enhanced tortuosity in crack paths, especially in the finer microstructures, results in the phenomenon of brick pull-out – this is particularly noticeable for the 200 μm brick

size, which results in significant crack bridging. As in nacre [39], this is likely to be the primary toughening mechanism in these structures. Specifically, the finer the structure the more tortuous the observed crack paths, with the 200 μm series having extensive crack deflection and brick pullout. Indeed, both of these extrinsic toughening mechanisms, *i.e.*, crack deflection and brick pull-out/crack bridging, are characteristic of natural nacre, and contribute to the steeply rising R-curve behavior of these nacre-like ceramic-Ni hybrids.

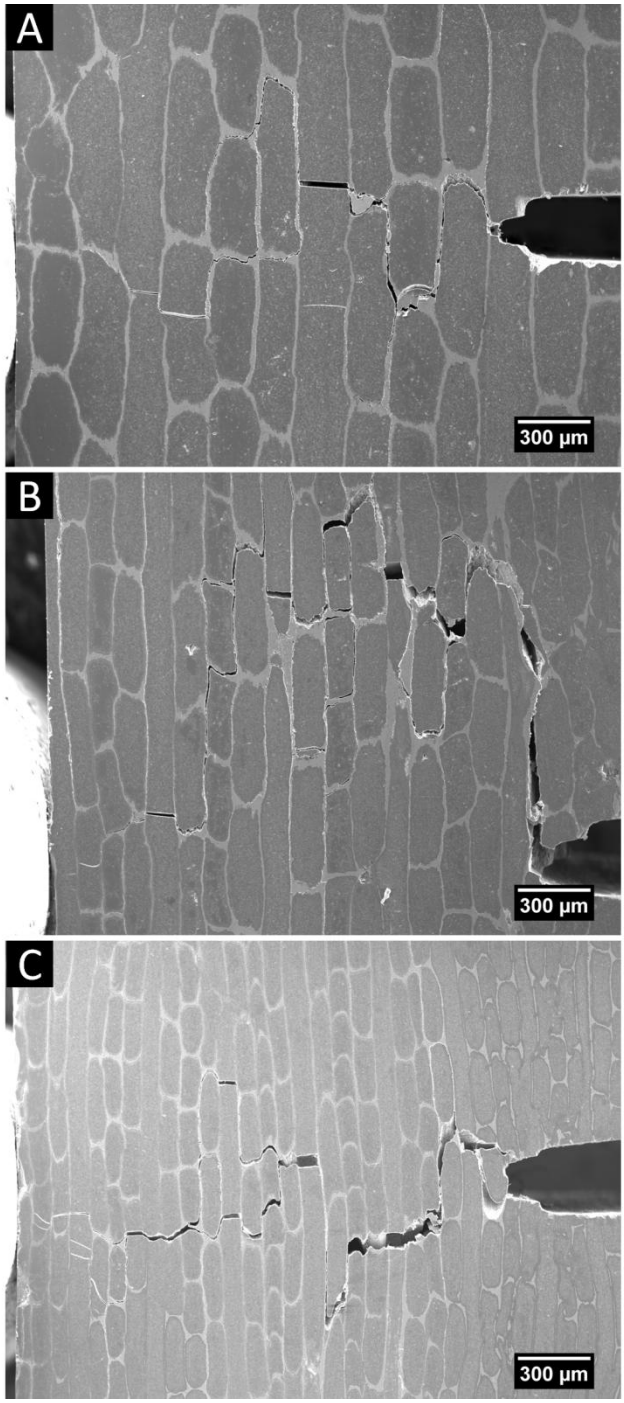


Figure 5.4: Scanning electron micrographs of one of the 500 µm (**A**), 300 µm (**B**), and 200 µm (**C**) specimens after *in situ* fracture analysis. In the 500 µm specimen, crack deflection can be seen above and below the crack root, with minimal cracking through the bricks. While the 300 µm specimen shows significantly more crack deflection above the crack root with noticeable crack bifurcation and crack bridging this is region. Finally, in the 200 µm sample the crack deviates somewhat from the plane of maximum tensile stress as there is extensive mortar delamination and crack deflection as well as multiple bricks bridging the crack path.

Crack deflection is also quite significant in these structures, although this invariably occurs via interfacial delamination, as can be seen in **Figure 5.5** where there is little to no evidence of ductile failure in the mortar. Limited "inter-brick" displacements are essential to create ductility (and hence toughness); however, to utilize the increased shear/tensile resistance of the metallic mortar for optimum toughness, such displacements would be better achieved within the mortar, rather than along mortar/brick interfaces.

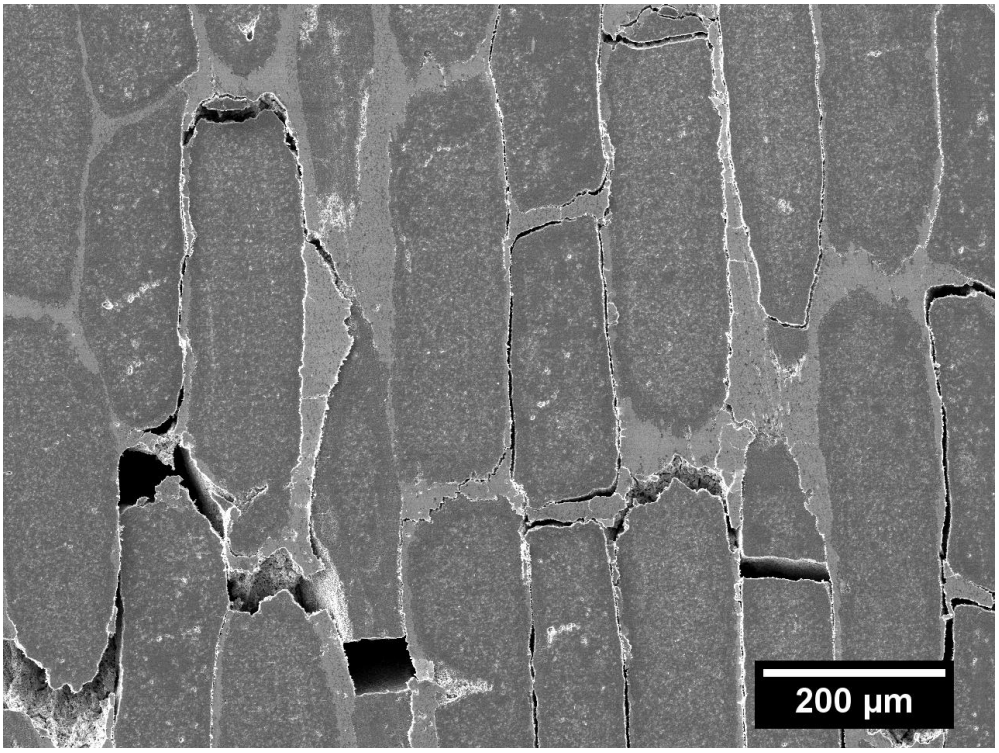


Figure 5.5: SEM micrograph of a 300 µm specimen showing the extent of interfacial delamination in the crack wake. While the inclusion of a metallic mortar was intended as a means of introducing a ductile failure mechanism into the structure, when weak interfaces are present there is little evidence of plasticity in the failure region and the crack travels along the interface instead. This behavior is inherent in all three structures produced by this method.

To gain some bearing as to how weak these mortar/brick interfaces in these structures are, the He and Hutchison [75] analysis was used. This defines the (elastic) conditions for an impinging crack to either penetrate through a dissimilar material interface or arrest/delaminate along the interface, and as such can be used to estimate the interfacial toughness [76] (**Figure 5.6**). Two factors determine whether or not the crack will delaminate along the interface: (i) the elastic mismatch of the two materials, given by the first Dundurs' parameter, $\alpha = (E_1 - E_2)/(E_1 + E_2)$, where E_1 and E_2 are the Young's moduli of the two materials [77], and (ii) the ratio of the interfacial toughness to the toughness of material 2 which the crack would enter if it penetrated the interface, $\mathcal{G}_{c,interf}/\mathcal{G}_{c2}$, where toughness values are expressed in terms of the strain energy release rate $\mathcal{G}$. For a crack originating in the alumina traveling into the nickel mortar, $\alpha \sim -0.26$, the estimation of an upper-bound for the toughness of the interface is given by $\mathcal{G}_{c,interf}/\mathcal{G}_{c2} \sim 0.23$. This was confirmed by creating a Vickers indent at a load of over 10 N in the alumina to generate cracks which are directed to impinge roughly normally on the nickel/alumina interface

(**Figure 5.6**); these cracks can be seen to not penetrate the interface but rather to become arrested and form interface delamination cracks. Using a value of 0.031 kJ/m^2 for the toughness of the alumina, **Table 5.2** lists the data measured using this approach, which gives an upper-bound estimate of the interfacial toughness of 21.8 kJ/m^2.

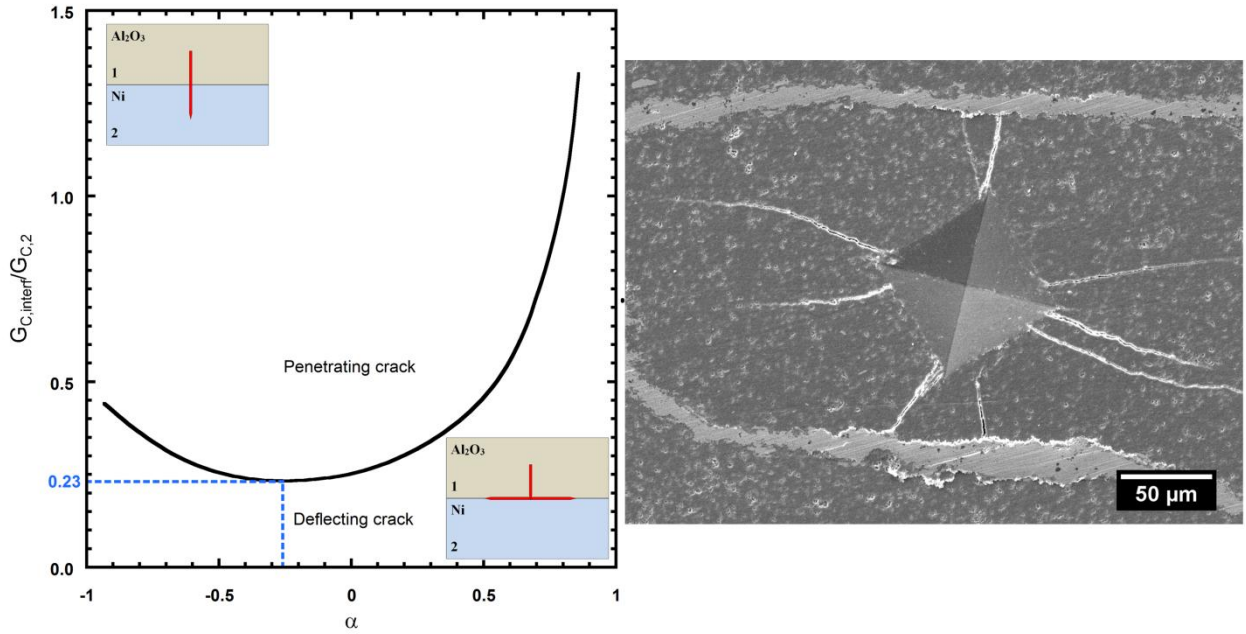


Figure 5.6: A plot of the linear elastic solutions of He and Hutchison [75] which show the conditions where a crack impinging normally on a dissimilar material interface between materials 1 and 2 will either penetrate the interface or arrest/deflect along the interface. For a ~90° incident crack angle, two factors determine whether or not the crack will penetrate: (i) the elastic mismatch between the two materials which is given by the first Dundurs' parameter $\alpha = (E_1 - E_2)/(E_1 + E_2)$, where E_1 and E_2 are the Young's moduli of the two materials [77], and (ii) the ratio of the interfacial toughness to the toughness of material 2 which the crack would enter if it penetrated the interface, $\mathcal{G}_{c,interf}/\mathcal{G}_{c2}$. For a penetrating crack originating in the alumina traveling into the nickel mortar, $\alpha \sim -0.26$. If cracks emanating from Vickers hardness indents in the alumina are directed to impinge normally on the nickel/alumina interface, as the right-hand micrograph shows they do not penetrate the interface but rather form delamination cracks along the interface. This allows for the estimation of an upper-bound toughness of the nickel/alumina interface of $\mathcal{G}_{c,interf} \sim 0.23$.

Table 5.2: Tabulated data for the interfacial toughness, determined using the He-Hutchinson analysis [75].

	Toughness, $\mathcal{G}_C$ (kJ/m^2)*	**Toughness, K_{Ic} (MPa.m$^{1/2}$)**
Al_2O_3	0.031	3.49
Nickel	94.2	146.9
Al_2O_3/Ni Interface	< 21.8	-

* K_{Ic} values for alumina were measured directly in this study, whereas a value for the toughness of nickel was taken from ref. [78]. These values were then converted to strain energy release rates ($\mathcal{G}_C$). It should be noted that the interfacial toughness can only be determined as an upper-bound.

5.2. DISCUSSION

Coextrusion is a unique processing method that can be used to make, and subsequently tune, the architecture of nacre-like, brick-and-mortar ceramic-metal hybrid structures through the production of mortar-coated ceramic filament. Methods such as chopping the filament into individual bricks as well as compressing them individually to further increase the aspect ratio have been explored in detail previously [79]. However, it was found that simply laying up the filament layer by layer at variable offset angles was particularly effective at producing brick-and-mortar architectures, but also in developing desired mechanical properties, in particular crack-growth resistance in terms of inhibiting catastrophic fracture from unstable growth of incipient cracks. This was related to a combination of two factors: a high degree of mortar interconnectivity and the increase in the brick aspect ratio via the brick length. Adjusting the filament diameter was the next logical progression for the development of these brick-and-mortar architectures. Varying the filament diameter provided a means to reduce the overall brick size without the detrimental effects of limited mortar interconnectivity that were seen previously using additional manipulation of the filament post extrusion [79]. Accordingly, three microstructures were produced by the filament layup method with excellent looking brick-and-mortar structures, with brick sizes varying between 500 and 200 μm (**Figure 5.1**).

The structure of these coextruded alumina-Ni hybrids, while mimicking the relative proportion of bricks to mortar in nacre, are obviously far coarser than the natural material. In terms of properties, this is reflected in their low flexural strengths which, as in our previous study [79], remain under 200 MPa. This is clearly a drawback with coextrusion processing although the current results unambiguously indicate that both strength and toughness properties are improved by refining the brick size. The advantage of coextrusion though is that it enables the processing of seemingly perfect, albeit coarse, model brick-and-mortar structures in the true image of nacre with a high-volume fraction of ceramic exceeding 90% together with a metallic mortar. Based on micromechanical modeling [36], this should represent the ideal structure, and indeed these alumina-Ni hybrids do display excellent toughness with R-curve fracture toughness values exceeding 15 $MPa.m^{½}$; this is the highest fracture toughness reported to date for a high-volume fraction alumina with a metallic compliant phase. This is achieved by the relative absence of brick fracture, and the occurrence of shear displacements in the mortar regions, leading to crack deflection, crack-path tortuosity, brick pull-out and consequent crack bridging. As in nacre [39], such bridging is likely to be the primary toughening mechanism, resulting in the steep rising R-curve behavior in these structures (**Figure 5.3**). This stabilizes the subcritical extension of cracks, thereby avoiding unstable catastrophic failure of the ceramic. However, one must still question why these toughness values, although high, still do not approach the levels attained using brick-and-mortar alumina structures containing a polymeric (PMMA) mortar where measured toughness values were significantly larger [4].

The reason for this appears to be that although both the polymer and metallic mortars provide for inter-brick displacement to minimize brick fracture, which initiates the brick pull-out that is the origin of toughening by crack bridging, these displacements occur *within* the mortar when polymers are used as the compliant phase, whereas in the present case with a Ni mortar, the majority of the inter-brick displacement takes place along the Ni-alumina interface rather than within the metallic phase. It should be noted that polymer/PMMA interfaces were intentionally made strong, using techniques such as grafting [9,80], to force the inter-brick displacements to

occur within the mortar, where the toughening can be augmented by the creation of damage in the layer and additionally by the resistance of the mortar itself to shear (and also tension for the vertical mortar regions). The potentially enhanced toughening effect of a metallic mortar is in its greater strength, in terms of higher resistance to tension and shear, as compared to a polymer like PMMA, although the mortar strength cannot, of course, exceed the strength of the ceramic or else brick fracture would ensue, which would completely compromise the strength and toughness of the material. Inter-brick displacements along the ceramic/mortar interfaces, as with the present materials, still protect the bricks from fracture and as such create the conditions for toughening by crack deflection and bridging, but such cracking along the interfaces serves to curtail the additional toughening from the shear/tensile resistance of the mortar. Indeed, this is also the prime reason for the lower strength of our materials.

To determine why the nickel/alumina interface was much weaker than the nickel, further examination was performed to measure the maximum interfacial toughness; a value of ~21.8 kJ/m^2 was obtained which is, at best, less than 25% of the toughness of nickel. Further investigation using SEM analysis yielded interesting results when comparing secondary to backscatter images where backscatter can produce higher elemental contrast. **Figure 5.7** shows a noticeable difference between the secondary (A) and backscatter (B) images, specifically the presence of an intermediate region between the nickel and alumina. High-resolution images of this region (D) show that it consists of alumina grains with interdispersed nickel along the grain boundaries, likely a remnant of the decomposition reaction of Al_2NiO_4 spinel during processing. Cracks travel primarily along the interface between the nickel and the reaction region (C), but it is not clear if the presence of this reaction region is the cause of the weak interface, as highly tortuous interfacial regions between nickel and alumina have been attributed in the past to reduced mechanical performance [81].

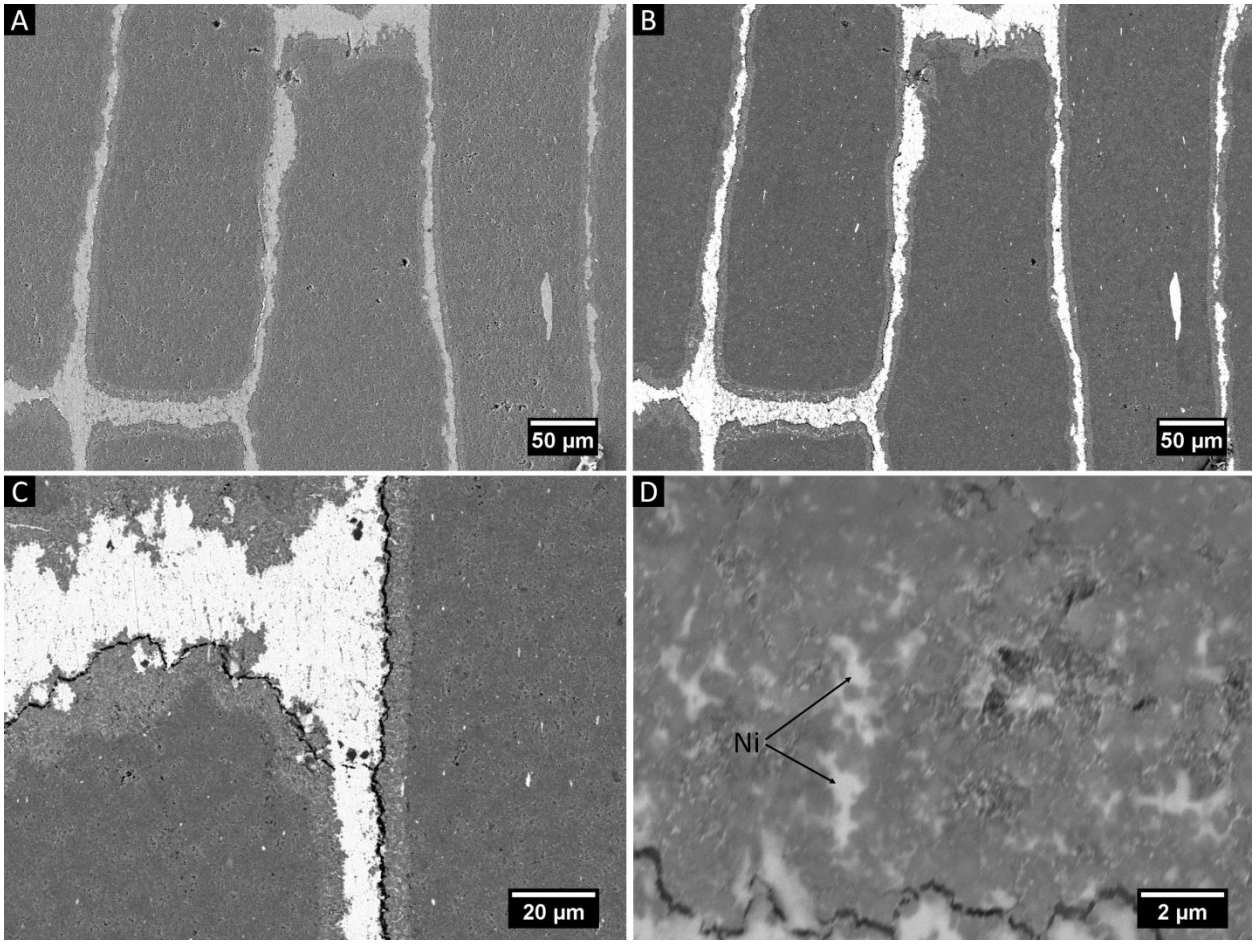


Figure 5.7: Comparison SEM micrographs imaged using secondary electron (SE) imaging (**A**) and backscatter (BSE) electron imaging (**B**) showing the presence of a region between the alumina bricks and nickel mortar. Backscatter images (**C**) show that the cracks traverse along the interface between the reaction region and the nickel mortar; higher-resolution imaging (**D**) indicates that the region is comprised of alumina grains with the nickel in the grain boundaries providing the higher elemental contrast with BSE. This is likely a remnant of the decomposition reaction that occurs during the final heat treatment to reduce the nickel aluminate spinel formed during sintering back into nickel and alumina.

What we learn from this is that to create lightweight structural materials with >90 vol.% ceramics materials using bioinspired (nacre-like) brick-and-mortar structures, the use of metallic mortars offers the greatest potential, both in terms of its higher temperature capability and that theoretically it should attain higher strength and toughness; however, to realize such high toughness without diminishing strength, it will be necessary to not only refine the brick widths to less than 10 μm or so, which incidentally would be difficult using the coextrusion methodology, but also to develop such ceramic/compliant metal phase structures where the ceramic/metal interface is strong enough for the inter-brick displacements to be confined within the metal mortar, yet not too strong to cause brick failure. To date, no one has achieved this ideal bioinspired structure.

5.3. SUMMARY

In this study, using coextrusion we have developed and processed a nacre-like brick-and-mortar architecture of an alumina (brick-like) microstructure containing a metallic nickel compliant (mortar) phase, where we have been able to refine the ceramic brick size by varying the coextruded filament diameter. While coextrusion produces structures that are significantly courser than naturally-occurring nacre, these drawbacks are somewhat mitigated by the high degree of tunability that can be achieved. The method enabled the production of >90 vol.% ceramic brick-and-mortar microstructures, containing a <10 vol.% metallic mortar and bricks ranging in size from ~180 to 430 μm, that exhibit marked crack-growth resistance with toughness values exceeding 15 MPa.m^{½} (compared to values of ~5 MPa.m^{½} for monolithic alumina. The resulting nacre-like alumina-nickel structures processed in this study all exhibited:

- significant resistance to crack growth and failure, *i.e.,* steeply rising R-curve behavior,
- strength, crack-initiation K_{Ic} toughness and crack-growth toughness on the R-curve that increased with decreasing brick size,
- R-curve toughness exceeding 15 MPa.m^{½}.

Although the present model alumina/Ni-metal brick-and-mortar structures are clearly coarse, they nevertheless displayed excellent toughness compared to monolithic alumina, but with low flexural strength. However, we believe that these structures have the potential with metallic mortars to achieve significantly higher toughness and strength. This is because in the present materials, the limited inter-brick displacements, which are absolutely vital to attain the required toughness by stabilizing subcritical cracking without catastrophic fracture, largely occurred along the ceramic-metal interfaces. To utilize the full potential of the shear/tensile strength of metallic mortars, these inter-brick displacements need to be within the mortar, which can only be effectively achieved by finding a means of strengthening these biomaterial interfaces. This will both significantly elevate the strength and potentially further enhance the already high toughness of these compliant-phase ceramics.

Chapter 6
Elevated Temperature Mechanical Properties

6.1. RESULTS

6.1.1. Mechanical Characterization – Strength

Four-point flexural tests were performed in a fully articulating SiC fixture to determine the flexural strength of the 200 µm series of microstructures with the results shown in **Figure 6.1**. These strength tests were performed at 100°C intervals starting at 600°C and ending at 900°C where the test temperature exceeded 2/3 the absolute melting point of the nickel (879°C). A slight increase in strength can be seen between room temperature (158±24 MPa) and 700°C (175±15 MPa), followed by a small drop in strength at 800°C (158±21 MPa) and a much more significant drop at 900°C (111±15 MPa) which was expected. Considering that pure alumina does not see any significant reduction of flexural strength between room temperature and 900°C [82], the changes in strength for this compliant phase ceramic are due to the nickel metal along the brick boundaries.

6.1.2. Mechanical Characterization – Toughness

Toughness was evaluated at elevated temperature for this material using a J_R-curve analysis as detailed in Section 3.3., specifically through an indirect crack length measurement unlike the previous chapters in which a direct method was used. This was considered to be more valuable than simply producing K_{Ic} initiation toughness as these materials have been shown to have toughness evolution and hence a singular value does not fully encompass the full toughening behavior of the material. Micro-notched three-point flexural samples were loaded at temperature while strain was directly measured on the tensile surface using an LVDT while compliance evolution was determined through loading and unloading cycles as failure was occurring. The K_J *R*-curves are presented in **Figure 6.2** and notably show little to no change between room temperature and 600°C, with a maximum "valid" toughness of 8 MPa.m$^{1/2}$. From there the 700°C curve rises to 9 MPa.m$^{1/2}$ and even further at 800°C to almost 13 MPa.m$^{1/2}$, after which the 900°C shows a drop back to around 9 MPa.m$^{1/2}$. It should be noted that although these are the maximum "valid" ($\Delta a_{max} = 0.25 b_0 = 550$ µm), the *R*-curve data continues to trend upwards beyond that, notably with the 800°C series seeing a maximum of 16 MPa.m$^{1/2}$.

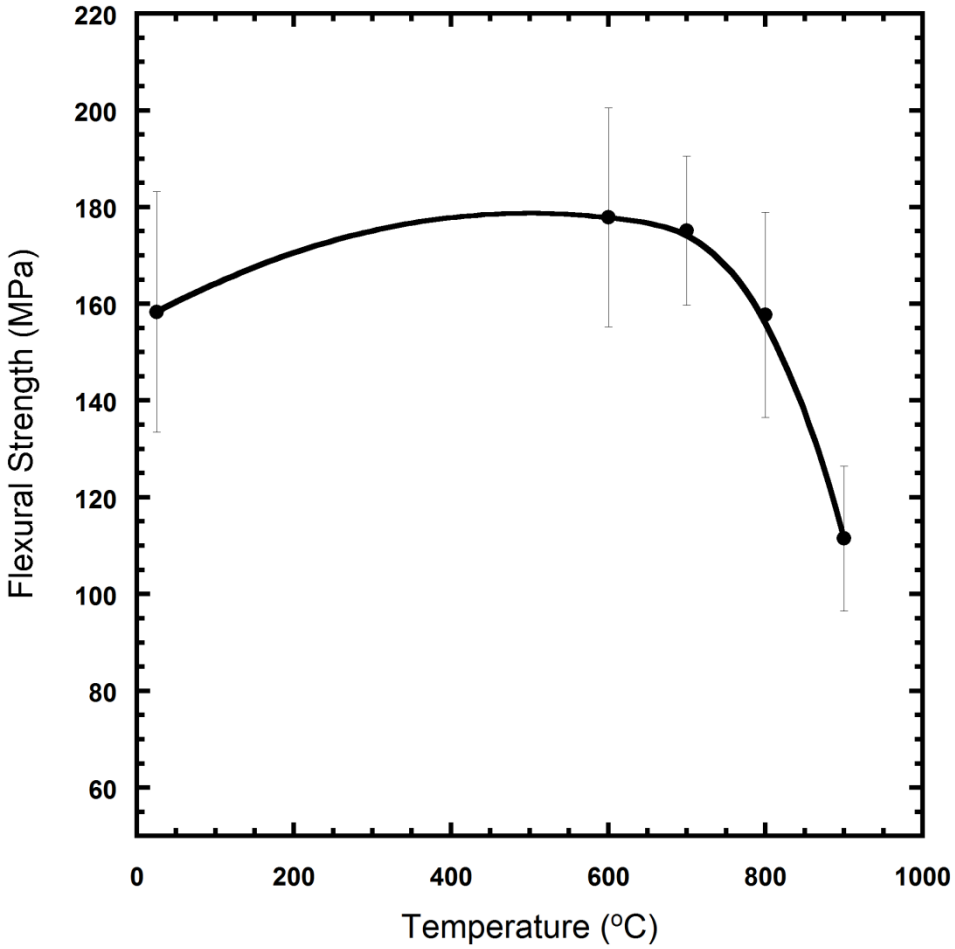


Figure 6.1: Flexural strength produced via 4-point bending of the 45° offset brick-and-mortar structure produced with 200 µm filament. Strength gradually increases from room temperature to 600°C, likely due to reduction of residual stresses from Al_2O_3 and Ni thermal expansion mismatch, while a decrease in strength is seen after 700°C with the drop in strength accelerating after 800°C.

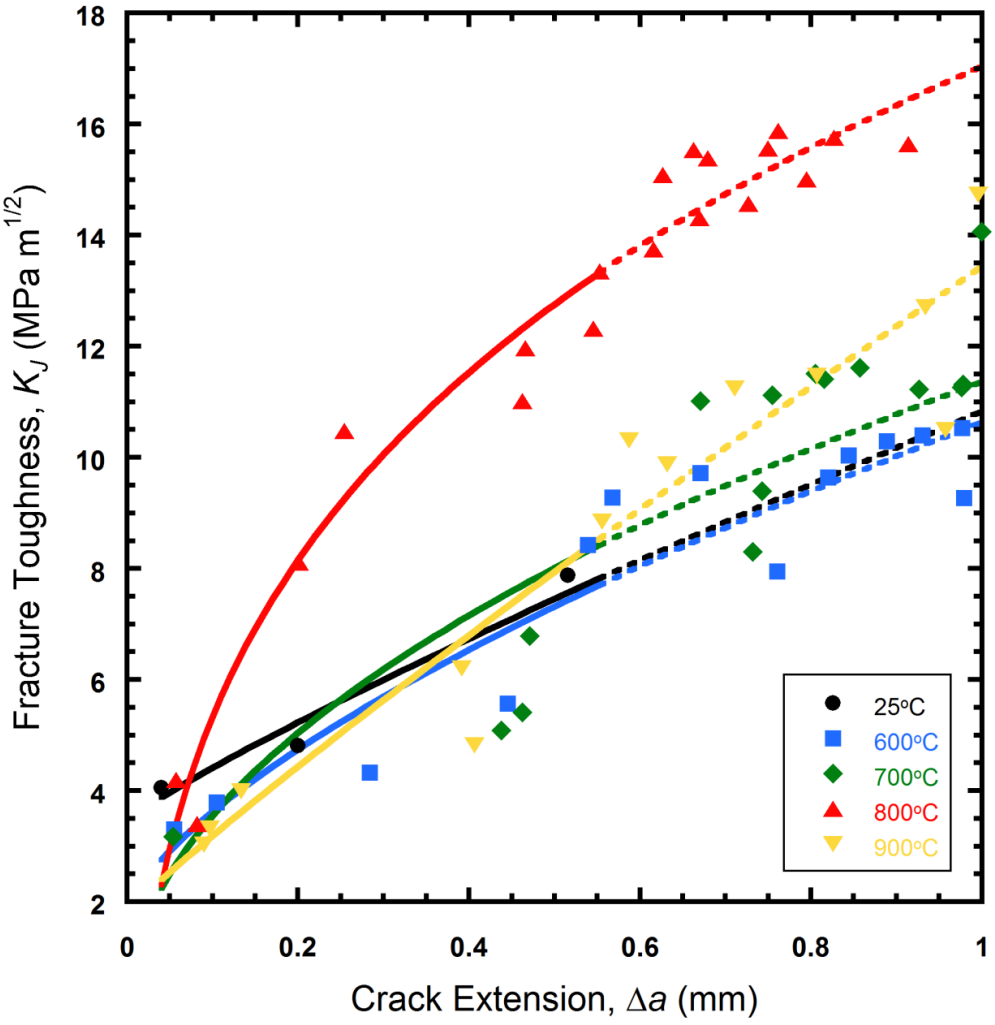


Figure 6.2: *R*-curves the coextruded brick-and-mortar structure at room temperature, 600, 700, 800, and 900°C. Room temperature and 600°C have almost identical curves, with a small increase at 700°C. This is followed by a marked increase at 800°C where ductile mortar behavior is believed to engage instead of interfacial mortar/brick failure. The *R*-curve then drops again at 900°C, with correlates with a significant drop in strength from **Figure 6.1**, meaning that the temperature has compromised all mechanical properties at that point.

These *R*-curve values at face value seem to be less than those seen in the previous chapter at room temperature, but the different method of measuring them inherently leads to a more conservative data set. The method of cyclically loading and unloading the specimens to ascertain the compliance evolution can lead to microcrack extension, producing Δa values that are artificially larger for the load in which the crack naturally extended. This results in shallower *R*-curves which is confirmed in **Figure 6.3**, in which room temperature *R*-curves were produced for identical 200 µm filament specimens: one with this indirect method and another with the direct *in-situ* method used in the previous chapters.

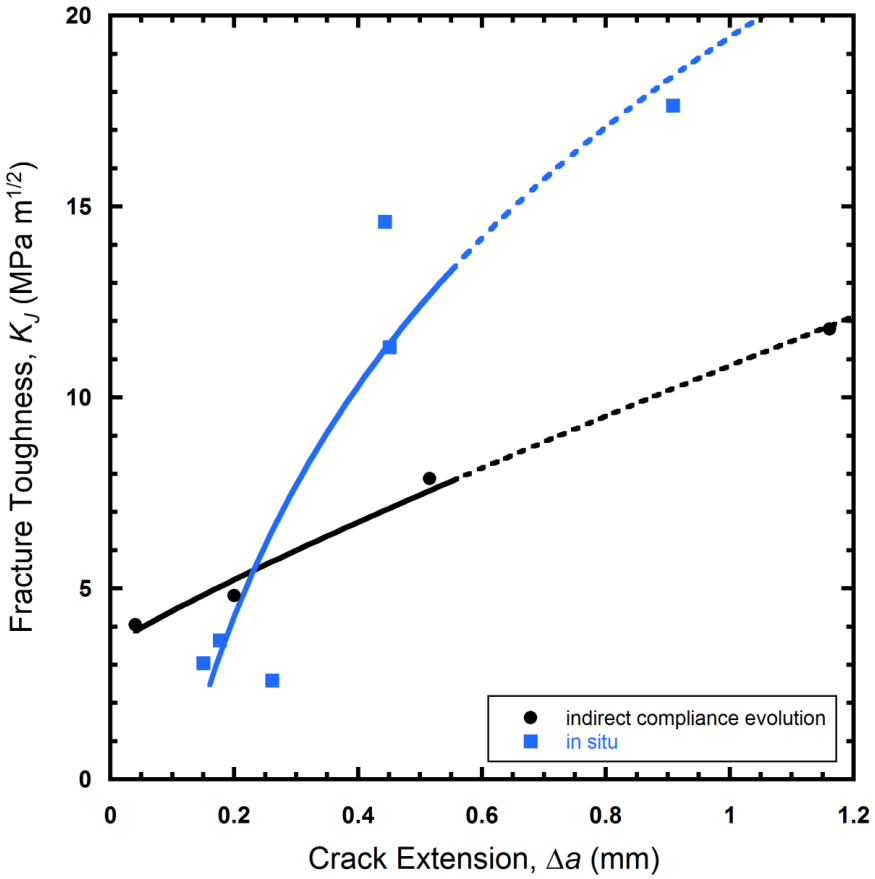


Figure 6.3: *R*-curves produced at room temperature for the same 200 µm coextruded structures, one with in *in-situ* SEM method used in the previous chapters while the lower curve is produced with the indirect method that uses compliance evolution to determine the crack length. The indirect method has a noticeably lower curve, which is due in part to microcracking that occurs during the unloading cycle necessary to determine the change in compliance. Microcracking during unloading will extend the Δa, which extends out the curve, lowering it in comparison to the *in-situ* method that the crack length at the exact point in load that it extends. This produces a more conservative curve, but because all the *R*-curves in **Figure 6.2** are measured using the method, the comparisons are self-contained and valid.

6.1.3. Crack Growth Observations

Observations were performed to relate crack growth behavior with the corresponding *R*-curves for each temperature in this series. **Figure 6.4** shows crack pathways observed in all of the elevated temperature specimens. Crack deflection is significant in all of these structures, which indicates that at least all of the extrinsic toughening effects (bridging, deflection, wedging, etc.) have not be degraded by the increased temperature. In the 600°C and 700°C images similar behavior can be seen to room temperature samples of the same material (**Figure 5.5**); specifically, cracks that pass through the brick phase and cracking along the Al_2O_3/Ni interface that has plagued these structures since their initial fabrication, indicating that toughening behavior is still strictly extrinsic at least through 700°C and that the mortar has little or no impact outside of providing a weak interface to direct fracture along. However, at 800°C and 900°C there is a welcome change: cracking can be seen to be fully contained within the mortar and not along the mortar/brick interface. This is therefore a full actualization of brick and mortar

behavior observed in a metal complaint phase ceramic, albeit at a temperature in which the ductility of the metal is maximized. A final point to clarify is that there is significant oxide scale present in the 900°C specimen, which could be a contributing factor in the degradation of strength and *R*-curve behavior seen in **Figures 6.1** and **6.2**.

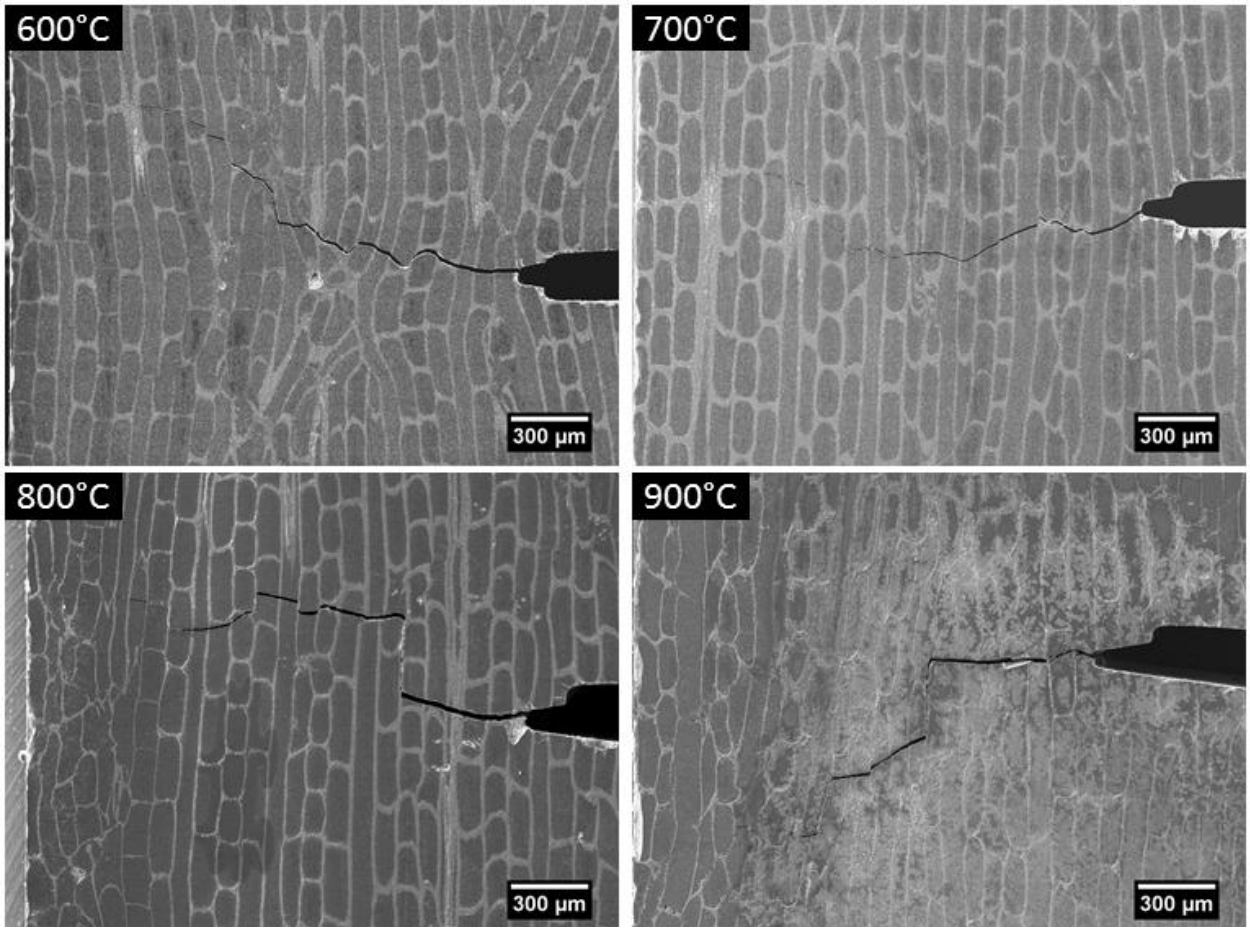


Figure 6.4: Crack pathways from fracture toughness specimens seen at each of the elevated temperatures. Both the 600°C and 700°C samples had fracture pathways that were identical to room temperature pathways seen in the last chapter, with the crack either failing through bricks or along the brick-mortar interface. The specimens at 800°C and 900°C can be seen to have cracking within the nickel mortar which corresponds to the larger increase in *R*-curve behavior seen in **Figure 6.3**.

6.2. DISCUSSION

Coextrusion has shown as a successful processing route for the production of synthetic brick and mortar architectures with low metallic content. Over the course of the last two studies [REF] the role of brick morphology, mortar interconnectivity, and the size of the bricks have been explored in their relationship to the mechanical performance of this material system. While the attempts to mimic the natural toughening mechanisms of nacre have been mostly successful, the dominance of weak interfacial failure of the brick and mortar interfaces has been a persistent issue plaguing these systems. This has limited the performance of the coextruded brick-and-mortar systems by restricting the toughing mechanisms to only the extrinsic ones (crack deflection, bridging, wedging, etc.) and none of the intrinsic toughening ideally provided from the ductile mortar phase. This behavior arises as a consequence of the interfacial shear strength of the Al_2O_3/Ni interface being weaker than the yield strength of the nickel. Therefore, there is the potential that there is a point in temperature at which the yield strength of the nickel drops below that of this interfacial strength, and hence engaging the full suite of toughening mechanisms that have been predicted in these metal compliant phase ceramic materials.

Elevated temperature flexural strength tests were performed to on 200 μm filament coextruded brick-and-mortar microstructures to determine the acceptable temperature range in which to do *R*-curve analysis as well as to explore what other effects temperature might have. **Figure 6.1** shows the results of the high temperature flexural tests, with two notable features. First, there is a small increase in strength between room temperature and 700°C. Most materials see decreasing strength as a function of temperature, and while notable exceptions, such as graphite, exist, this is likely due to an extrinsic factor. Residual stresses from the thermal expansion mismatch of nickel (13.1 μm/m-°C at RT) and alumina (5.5 μm/m-°C at RT) as a result of sintering the structure at 1400°C. These stresses would be minimized upon testing at a higher temperature, leading to the results seen in **Figure 6.1**. The other notable trend is a slight drop in strength of 20 MPa at 800°C followed by a more dramatic drop of 45 MPa at 900°C. This is a result of the steady decrease the yield strength of the nickel, which has been shown to reduce by more than 75% of its room temperature strength before reaching 900°C [83]. These results indicate that this materials maximum operable temperature is around 800°C before the mechanical properties start to deteriorate rapidly and gives an indication as to how the microstructure could responding during failure.

Crack growth resistance curves, as well as microscropy provide further insight on the high temperature failure mechanisms present in the structure. Rising *R*-curves indicate toughness evolution, similar to what has been reported on previously, with steeper and higher curves been produced with increasing temperature. This maximizes at 800°C, where the flexural strength was just starting to deteriorate a small degree from the baseline, followed by dropping *R*-curve behavior at 900°C mimicking the strength performance as well. **Figure 6.4** shows crack pathways typical for the four elevated temperatures, with the notable difference that the 800°C and 900°C specimens show cracking contained within the nickel mortar while the 600°C and 700°C do not. This is further examined in **Figure 6.5** where higher magnification images of the 800°C specimens. There is significant evidence of ductile tearing, with little cracking occurring along the Al_2O_3/Ni interface. Given the high temperature yield strength data of nickel [REF], this indicates that at 800°C the shear strength of the interface is less than 25 MPa, which is the yield

strength of pure nickel at that temperature. However, at that high of a temperature, little to no strain hardening occurs before ultimate failure based off of the yield and tensile strength data of nickel [REF]. This reduces a possible avenue for even further increased damage tolerance through the yielding and subsequent hardening of the mortar before eventual crack propagation.

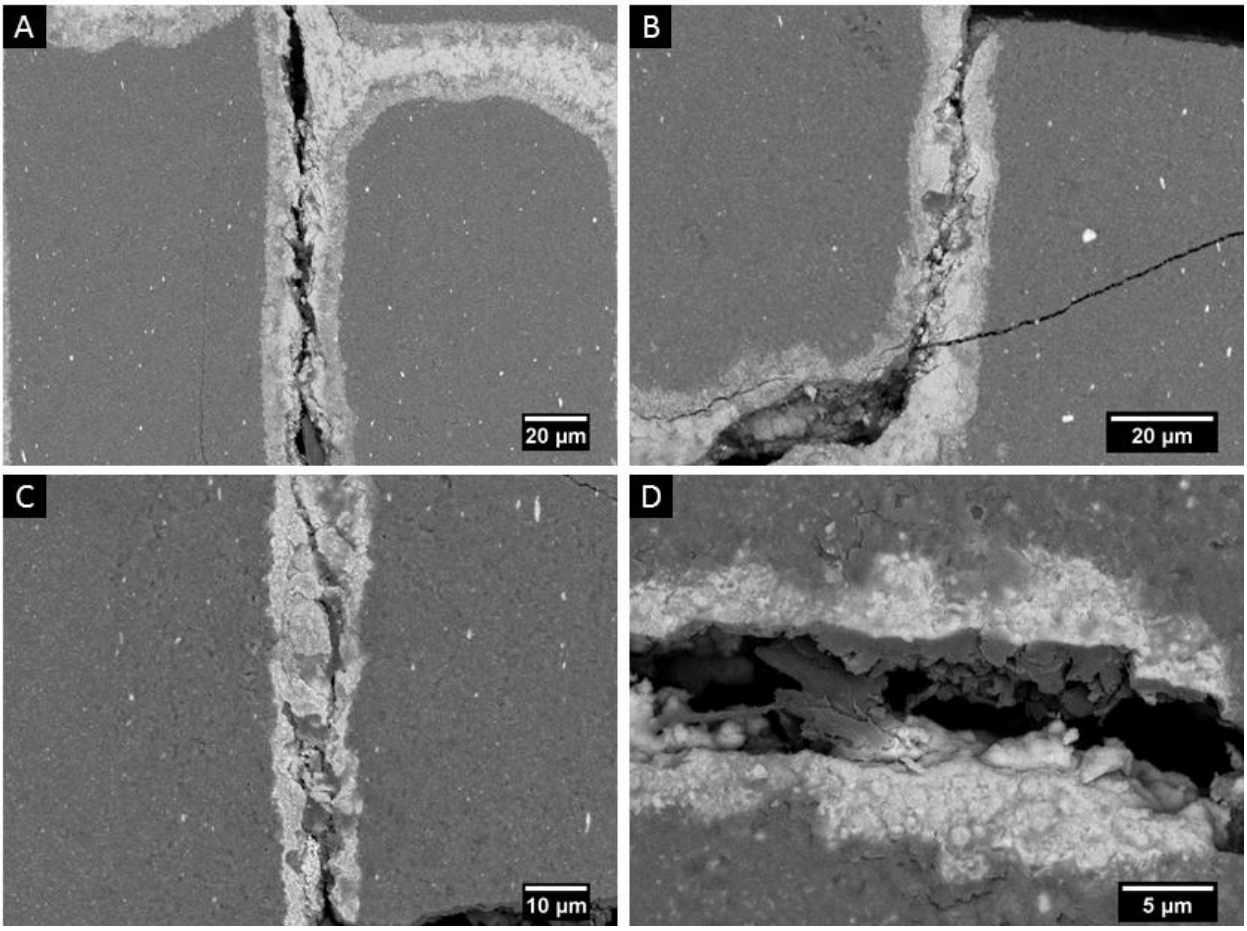


Figure 6.5: Scanning electron images taking in backscatter electron (BSE) imagining mode to enhance the contrast between the Al_2O_3 bricks and Ni mortar of samples broken at 800°C. (**A**) and (**B**) show cracks contained within the mortar, with little to no interfacial cracking being present. (**C**) and (**D**) have evidence of ductile tearing and bridging of the crack passing through the mortar.

High temperature mechanical data from these brick-and-mortar architectures suggest that they become more viable for structural applications as a function of increasing temperature. While most ceramics, including alumina [82], see reductions in toughness as temperature goes up, this class of ductile phase ceramics does quite the opposite while still maintaining strength on par with their room temperature alternative. Additionally, the more significant increase in *R*-curve behavior correlates to when the material changes from interfacial brick and mortar failure to ductile mortar failure coupled with the same extrinsic mechanisms.

6.3. SUMMARY

The mechanical performance of brick-and-mortar architectures made via coextrusion were examined at elevated temperatures in an attempt to circumvent weak interfacial effects. The improving *R*-curve behavior coupled with fracture analysis suggests that the decreasing yield strength of the nickel mortar improves the crack growth resistance by reaching a point where it allows ductile failure of the mortar before interfacial failure. Simultaneously, the flexural of the composite ceramic is not deteriorated in this same temperature regime, but is still reduced below that of pure ceramic. However, this is the first time in which a synthetic brick-and-mortar microstructure that has been produced with a ceramic brick and metallic mortar phase in which the full suite of intrinsic and extrinsic toughening mechanisms has been fully demonstrated.

While these results are limited to around 800°C, they do aid in determining new directions of potential future work. It has been suggested in previous papers that improving the interfacial strength above that of the mortar's yield strength should produce similar or better results than what was seen in this study. This would also have the added benefit of fully utilizing the plasticity of the metallic mortar through the strain hardening as a method of energy absorption. Another possible route for improving these metallic complaint phase ceramics would be to use a higher temperature alloy such as a nickel-based super alloy instead of the pure nickel. A super alloy would increase the operating temperature, allowing for a larger range of temperatures in which full brick-and-mortar behavior occurs, even if the interfaces are weak at room temperature.

Chapter 7
Conclusions and Suggested Future Work

One of the key factors to the development of synthetic brick-and-mortar structures is understanding how to effectively combine two or more dissimilar materials. While this is an issue that must be reconciled when making most composite materials, there are factors that make it a uniquely difficult challenge to overcome when making brick-and-mortar structures. The desired low volume fraction of mortar heavily restricts infiltration methods between wetting angle incompatibilities and penetration depth. High aspect ratio bricks means alignment methods are necessary for successful processing and the small feature size increases the amount of brick to mortar contact area, leading to mortar interconnectivity issues. These factors complicate the processing even further when attempting to use a metallic mortar instead of polymeric.

The study presented here is one of the first to synthesize metal compliant phase, brick-and-mortar structures with high (>90 vol. %) ceramic content. While the microstructures made this way have bricks an order of magnitude larger than naturally occurring nacre, the coxtrusion method is proven to be a versatile way to tune the brick size and morphology. It has been shown that mortar contiguity plays a pivotal role in the engagement of the brick-and-mortar toughening mechanisms, and it will become a limiting factor as further advances are made into low metallic content brick-and-mortar structures. Additionally, reduced feature size improves strength, toughness, and crack growth resistance behavior. This gives insight into the mechanical performance of brick-and-mortar structures on the desired size scale of nacre, even though the ones made here were far courser.

This study for the first time provides evidence of ductile mortar behavior in metal mortar brick-and-mortar ceramics. Many of the models that predict the mechanical behavior of thesis synthetic brick-and-mortar structures assume that strong interfacial bonding will be present between the mortar and brick. However, it was found that interfacial failure dominates the failure behavior and will likely be a hurdle for future metallic compliant phase brick-and-mortar ceramics. In this study it was possible to bypass issues that arise from interfacial failure by testing at higher temperatures where the mortar yield strength drops below the interfacial strength. At this point the full suite of brick-and-mortar intrinsic and extrinsic toughening effects are engaged, confirming that the models are accurate in regards to improved performance when failure is contained within the mortar. Not only is this study the first to do a comprehensive study of low metallic content brick-and-mortar structures but also the first to show the improved crack growth resistance when the metallic mortar is fails in a ductile manner.

The three studies that comprise this larger body of work provide insight into the future design and development of metal-compliant phase brick-and-mortar ceramics. Reducing the brick size while maintaining a high level of mortar interconnectivity should improve mechanical performance, while improving the interfacial strength to greater than the mortar's yield strength will also lead to improved properties. This can be done through the inclusion of an intermediate material between the ceramic brick and metallic mortar that can strongly bond to both materials or by considering new combinations of brick and mortar materials in an attempt to work more compatible pairings. Another route would be to focus solely on high temperature mechanical

properties and extending the temperature range in which the full suite of brick-and-mortar toughening behavior is engaged. Refractory metals or certain superalloys would be the more obvious mortars to consider for these conditions, as well as exploring new ceramic phases that can have improved bonding with these high temperature metals.

References

[1] U.G.K. Wegst, H. Bao, E. Saiz, A.P. Tomsia, R.O. Ritchie, Bioinspired structural materials, *Nature Mater*. 14 (2015) 23-36.

[2] U.G.K. Wegst, M.F. Ashby, The mechanical efficiency of natural materials, *Philos. Mag*. 84 (2004) 2167–2181.

[3] C. Wang, Y. Huang, Q. Zan, H. Guo, S. Cai, Biomimetic structure design—a possible approach to change the brittleness of ceramics in nature, *Mater. Sci. Eng. C* 11 (2009) 9–12.

[4] E. Munch, M.E. Launey, D.H. Alsem, E. Saiz, A.P. Tomsia, R.O. Ritchie, Tough bio-inspired hybrid materials, *Science* 322 (2008) 1516-1520.

[5] O.O. Ekiz, A.F. Dericioglu, H. Kakisawa, An efficient hybrid conventional method to fabricate nacre-like bulk nano-laminar composites, *Mater. Sci. Eng. C* 29 (2009) 2050-2054.

[6] M.E. Launey, E. Munch, D.H. Alsem, E. Saiz, A.P. Tomsia, R.O. Ritchie, A novel biomimetic approach to the design of high-performance ceramic–metal composites, *J. Roy. Soc. Interface* 7 (2010) 741-753.

[7] F. Bouville, E. Maire, S. Meille, B. Van de Moortèle, A.J. Stevenson, S. Deville, Strong, tough and stiff bioinspired ceramics from brittle constituents, *Nature Mater*. 13 (2014) 508-514.

[8] V. Naglieri, B. Gludovatz, A.P. Tomsia, R.O. Ritchie, Developing strength and toughness in bio-inspired silicon carbide hybrid materials containing a compliant phase, *Acta Mater*. 98 (2015) 141-151.

[9] H. Bai, F. Walsh, B. Gludovatz, B. Delattre, C. Huang, Y. Chen, A.P. Tomsia, R.O. Ritchie, bioinspired hydroxyapatite/poly(methyl methacrylate) composite with a nacre-mimetic architecture by a bidirectional freezing method, *Adv. Mater*. 28 (2016) 50-56.

[10] H. Zhao, Y. Yue, L. Guo, J. Wu, Y, Zhang, X. Li, S. Mao, X. Han, Cloning nacre's 3D interlocking skeleton in engineering composites to achieve exceptional mechanical properties, *Adv. Mater*. 28 (2016) 5099-5105.

[11] J. Cairns, G.A. Plizzari, Y. Du, D.W. Law, C. Franzoni, Mechanical properties of corrosion-damaged reinforcement, *ACI Mater. J*. 102 (2005) 256-264.

[12] J.R. Scully, A. Gebert, J.H. Payer, Corrosion and related mechanical properties of bulk metallic glasses, *J. Mater. Res.* 22 (2007) 302-313.

[13] K. Sieradzki, R.C. Newman, Stress-corrosion cracking, *J. Phys. Chem. Solids* 48 (1987) 1101-1113.

[14] M. Creager, P.C. Paris, Elastic field equations for blunt crack with reference to stress corrosion cracking, *Int. J. Fract.* 3 (1967) 247-252.

[15] R.O. Ritchie, The conflict between strength and toughness, *Nature Mater*. 10 (2011) 817-822.

[16] J.W. Hutchinson, P.C. Paris, Stability analysis of J-controlled crack growth, *Elastic-Plastic Fracture, ASTM STP 668*, J.D. Landes, J.A. Begley, G.A. Clarke, Eds., American Society for Testing and Materials, (1979) 37-64.

[17] S.J. Garwood, J.N. Robinson, C.E. Turner, The measurement of crack growth resistance curves (R-curves) using the J integral, *Int. J. Fract.* 11 (1975) 528-530.

[18] M. Sakai, R.C. Bradt, The crack growth resistance curve of non- phase- transforming ceramics, *J. Ceram. Soc. Jpn.*96 (1988) 801-809.

[19] C.J. Gilbert, J.J. Cao, L.C. De Jonghe, R.O. Ritchie, Crack-growth resistance-curve behavior in silicon carbide: small versus long cracks, *J. Am. Ceram. Soc.*80 (1997) 2253-2261.

[20] N. Ramachandran, D.K. Shetty, "Rising crack-growth-resistance (R-curve) behavior of toughened alumina and silicon nitride, *J. Am. Ceram. Soc*. 74 (1991) 2634-2641.

[21] A.G. Evans, K.T. Faber, Crack-growth resistance of microcracking brittle materials, *J. Am. Ceram. Soc*. 67 (1984) 255-260.

[22] A.P. Jackson, J.F.V. Vincent, R.M. Turner, The mechanical design of nacre, *Proc. R. Soc. Lond. B* 234 (1988) 415-440.

[23] S.F. Gilbert, G.A. Loredo, A. Brukman, A.C. Burke, Morphogenesis of the turtle shell: the development of a novel structure in tetrapod evolution, *Evol. Dev.* 3 (2001) 47-58.

[24] W. Yang, I.H. Chen, B. Gludovatz, E.A. Zimmermann, R.O. Ritchie, M.A. Meyers, Natural flexible dermal armor, *Adv. Mater.* 25 (2013), 31-48.

[25] Y.S. Lin, C.T. Wei, E.A. Olevsky, M.A. Meyers, Mechanical properties and the laminate structure of Arapaimas gigas scales, *J. Mech. Behav. Biomed.* 4 (2011) 1145-1156.

[26] P.Y. Chen, J. Schirer, A. Simpson, R. Nay, Y.S. Lin, W. Yang, M.I. Lopez, J. Li, E.A. Olevsky, M.A. Meyers, Predation versus protection: fish teeth and scales evaluated by nanoindentation, *J. Mater. Res*. 27 (2012) 100-112.

[27] W. Yang, V.R. Sherman, B. Bludovatz, M. Mackey, E.A. Zimmermann, E.H. Chang, E. Schaible, Z. Qin, M.J. Buehler, R.O. Ritchie, M.A. Meyers, Protective role of Arapaima gigas fish scales: structure and mechanical behavior, *Acta Biomater.* 10 (2014) 3599-3614.

[28] W. Yang, B. Gludovatz, E.A. Zimmermann, H.A. Bale, R.O. Ritchie, M.A. Meyers, Structure and fracture resistance of alligator gar (Atractosteus spatula) armored fish scales, *Acta Biomater.* 9 (2013) 5876-5889.

[29] N. Guarin-Zapata, J. Gomez, N. Yaraghi, D. Kisailus, P.D. Zavattieri, Shear wave filtering in naturally-occurring Bouligand structures, *Acta Biomater*. 23 (2015) 11-20.

[30] J.C. Weaver, G.W. Milliron, A. Miserez, K. Evans-Lutterodt, S. Herrera, I. Gallana, W.J. Mershon, B. Swanson, P. Zavattieri, E. DiMasi, D. Kisailus, The stomatopod dactyl club: A formidable damage-tolerant biological hammer, *Science* 336 (2012) 1275-1280.

[31] L.K. Grunenfelder, N. Suksangpanya, C. Salinas, G. Milliron, N. Yaraghi, S. Herrera, K. Evans-Lutterodt, S.R. Nutt, P. Zavattieri, D. Kisailus, Bio-inspired impact-resistant composites, *Acta Biomater*. 10 (2014) 3997-4008.

[32] E.A. Zimmermann, M.E. Launey, H.D. Barth, R.O. Ritchie, Mixed-mode fracture of human cortical bone, *Biomaterials* 30 (2009) 5877-5884.

[33] E.A. Zimmermann, E. Schaible, H. Bale, H.D. Barth, S.Y. Tang, P. Reichert, B. Busse, T. Alliston, J.W. Ager III, R.O. Ritchie, Age-related changes in the plasticity and toughness of human cortical bone at multiple length scales, *P. Natl. Acad. Sci. USA* 109 (2012) 14416-14421.

[34] E.A. Zimmermann, B. Gludovatz, E. Schaible, B. Busse, R.O. Ritchie, Fracture resistance of human cortical bone across multiple length-scales at physiological strain rates, *Biomaterials* 35 (2014) 5472-5481.

[35] F. Barthelat, H. Tang, P.D. Zavattieri, C.M. Li, H.D. Espinosa, On the mechanics of mother-of-pearl: A key feature in the material hierarchical structure, *J. Mech. Phys. Solids* 55 (2007) 306-337.

[36] M.R. Begley, N.R. Philips, B.G. Compton, D.V. Wilbrink, R.O. Ritchie, M. Utz, Micromechanical models to guide the development of synthetic 'brick and mortar' composites, *J. Mech. Phys. Solids*, 60 (2012), 1545–1560.

[37] Y. Shao, H. Zhao, X. Feng, On flaw tolerance of nacre: a theoretical study, *J.R. Soc. Interface*, 11 (2014), 20131016.

[38] F. Barthelat, Designing nacre-like materials for simultaneous stiffness, strength and toughness: optimum materials, composition, microstructure and size, *J. Mech. Phys. Solids*, 73 (2014), 22–37

[39] Y. Shao, H.P. Zhao, X.Q. Feng, H. Gao, Discontinuous crack-bridging model for fracture toughness analysis of nacre, *J. Mech. Phys. Solids*, 60 (2012), 1400–1419.

[40] N. Sakhavand, R. Shahsavari, Universal composition-structure-property maps for natural and biomimetic platelet-matrix composites and stacked heterostructures, *Nat. Commun.* 6 (2015) 6523-6534.

[41] B. Ji, H. Gao, A study of fracture mechanisms in biological nano-composites via the virtual internal bond model, *Mat. Sci Eng. A* 366 (2004) 96-103.

[42] H. Zhao, Y. Yue, L. Guo, J. Wu, Y. Zhang, X. Li, S. Mao, X. Han, Cloning nacre's 3D interlocking skeleton in engineering composites to achieve exceptional mechanical properties, *Adv. Mater.* 28 (2016) 5099-5105.

[43] S. Deville, E. Saiz, R.K. Nalla, A.P. Tomsia, Freezing as a path to build complex composites, *Science* 311 (2006) 515-518.

[44] R.F. Guo, N. Guo, P. Shen, L.K. Yang, Q.C. Jiang, Effects of ceramic lamellae compactness and interfacial reaction on the mechanical properties of nacre-inspired Al/Al_2O_3-ZrO_2 composites, *Mat. Sci Eng. A* 718 (2018) 326-334.

[45] E. Munch, M.E. Launey, D.H. Alsem, E. Saiz, A.P. Tomsia, R.O. Ritchie, Tough, bio-inspired hybrid materials, *Science* 322 (2008) 1516-1520.

[46] M.E. Launey, E. Munch, D.H. Alsem, H.B. Barth, E. Saiz, A.P. Tomsia, R.O. Ritchie, Designing highly toughened hybrid composites through nature-inspired hierarchical complexity, *Acta Mater.* 57 (2009) 2919-2932.

[47] W. Cui, M. Li, J. Liu, B. Wang, C. Zhang, L. Jiang, Q. Cheng, A strong integrated strength and toughness artificial nacre based on dopamine cross-linked graphene oxide, *ACS Nano* 8 (2014) 9511-9517.

[48] H.L. Gao, S.M. Chen, L.B. Mao, Z.Q. Song, H.B. Yao, H. Colfen, X.S. Luo, F. Zhang, Z. Pan, Y.F. Meng, Y. Ni, S.H. Yu, Mass production of bulk artificial nacre with excellent mechanical properties, *Nat. Commun.* 8 (2017) 287-294.

[49] H. Zhao, Y. Yue, Y. Zhang, L. Li, L. Guo, Ternary artificial nacre reinforced by ultrathin amorphous alumina with exceptional mechanical properties, *Adv. Mater.* 28 (2016) 2037-2042.

[50] L.J. Bonderer, A.R. Studart, L.J. Gauckler, Bioinspired design and assembly of platelet reinforced polymer films, *Science* 319 (2008) 1069-1073.

[51] F. Bouville, E. Maire, S. Meille, B. Van de Moortèle, A.J. Stevenson, S. Deville, Strong, tough and stiff bioinspired ceramics from brittle constituents, *Nature Mater*. 13 (2014) 508-514.

[52] H. Le Ferrand, F. Bouville, T.P. Niebel, A.R. Studart, Magnetically assisted slip casting of bioinspired heterogeneous composites, *Nature Mater*. 14 (2015) 1172-1179.

[53] G. Hilmas, A. Brady, U. Abdali, G. Zywicki, J. Halloran, Fibrous monoliths: non-brittle fracture from powder-processed ceramics, *Mat. Sci Eng. A* 195 (1995) 263-268.

[54] J.W. Zimmermann, G.E. Hilmas, W.G. Fahrenholtz, Thermal shock resistance and fracture behavior of ZrB_2-based fibrous monolith ceramics, *J. Am. Ceram. Soc*. 92 (2009) 161-166.

[55] J. Watts, G.E. Hilmas, Processing and indentation behavior of functionally designed cellular cemented carbides produced by coextrusion, *Int. J. Refract. Met. H*. 24 (2006) 229-235.

[56] S. Baskaran, S.D. Nunn, D. Popovic, J.W. Halloran, Fibrous monolithic ceramics: I, fabrication, microstructure, and indentation behavior, *J. Am. Ceram. Soc*. 76 (1993) 2209-2216.

[57] C. Van Hoy, A. Barda, M. Griffith, J.W. Halloran, Microfabrication of ceramics by coextrusion, *J. Am. Ceram. Soc.* 81 (1998) 152-58.

[58] S. Baskaran, J.W. Halloran, Fibrous monolithic ceramics: II. Flexural strength and fracture behavior of the silicon carbide/graphite system, *J. Am. Ceram. Soc*. 76 (1993) 2217-2224.

[59] S. Baskaran, J.W. Halloran, Fibrous monolithic ceramics: III, Mechanical properties and oxidation behavior of the silicon carbide/boron nitride system, *J. Am. Ceram. Soc*. 77 (1994) 1249-1255.

[60] S. Baskaran, S.D. Nunn, J.W. Halloran, Fibrous monolithic ceramics: IV, Mechanical properties and oxidation behavior of the alumina/nickel system, *J. Am. Ceram. Soc*. 77 (1994) 1256-1262.

[61] D. Kovar, B.H. King, R.W. Trice, J.W. Halloran, Fibrous monolithic ceramics, *J. Am. Ceram. Soc*. 80 (1997) 2471-2487

[62] J. C. McNulty, M.R. Begley, F.W. Zok, In-plane fracture resistance of a crossply fibrous monolith, *J. Am. Ceram. Soc*. 84 (2001) 367-375.

[63] S.E. Landwehr, G.E. Hilmas, Strength of functionally designed cellular cemented carbides produced by coextrusion, *J. Mater. Sci.* 41 (2006) 8367-8371.

[64] R.W. Trice, J.W. Halloran, Elevated-temperature mechanical properties of silicon nitride/boron nitride fibrous monolithic ceramics, *J. Am. Ceram. Soc.* 83 (2000) 311-316.

[65] D.E. Aldrich, Z. Fan, P. Mummery, Processing, microstructure, and physical properties of interpenetrating Al_2O_3/Ni composites, *Mater. Sci. Tech.*16 (2000) 747-752.

[66] J. Gurland, The measurement of grain contiguity in two-phase alloys, *Trans. Met. Soc. AIME* 212 (1958) 452.

[67] Z. Fan, A.P. Miodownik, P. Tsakiropoulos, Microstructural characterisation of two phase materials, *Mater. Sci. Tech.* 9 (1993) 1094-1100.

[68] ASTM Standard C1161, 2013, Flexural strength of advanced ceramics at ambient temperature, ASTM International, West Conshohocken, PA, 2003, doi: 10.1520/C1161-13, www.astm.org.

[69] ASTM Standard E1820, 2016, Measurement of fracture toughness, ASTM International, West Conshohocken, PA, 2003, doi: 10.1520/E1820-16, www.astm.org.

[70] ASTM Standard C1259, 2015, Dynamic Young's modulus, shear modulus, and Poisson's ratio for advanced ceramics by impulse excitation of vibration, ASTM International, West Conshohocken, PA, 2003, doi: 10.1520/C1259-15, www.astm.org.

[71] C.A. Schneider, W.S. Rasband, K.W. Eliceiri, NIH Image to ImageJ: 25 years of image analysis, *Nat. Methods* 9 (2012) 671-675.

[72] X. Sun, J.A. Yeomans, Microstructure and fracture toughness of nickel particle toughened alumina matrix composites, *J. Mater. Sci.* 31 (1996) 875-880.

[73] J.J. Kruzic, R.M. Cannon, R.O. Ritchie, Effects of moisture on grain-boundary strength, fracture, and fatigue properties of alumina, *J. Am. Ceram. Soc*. 88 (2005) 2236-2245.

[74] W.G. Fahrenholtz, D.T. Ellerby, R.E. Loehman, Al_2O_3-Ni composites with high strength and fracture toughess, *J. Am. Ceram. Soc.* 83(2000) 1279-1280.

[75] M.Y. He, J.W. Hutchinson, Crack deflection at an interface between dissimilar elastic materials, *Int. J. Solids Struct*. 25 (1989) 1053-1067.

[76] V. Imbeni, J. J. Kruzic, G. W. Marshall, S. J. Marshall, and R. O. Ritchie, The dentin-enamel junction and the fracture of human teeth, *Nature Mater*. 4 (2005) 229-232.

[77] J. Dundurs, Discussion: Edge-bonding dissimilar orthogonal elastic wedges under normal and shear loading, *J. Appl. Mech*. 36 (1969) 650-652.

[78] A. Hohenwarter, R. Pippan, Fracture toughness evaluation of ultrafine-grained nickel, *Scripta Mater*. 64 (2011) 982-985.

[79] R.P. Wilkerson, B. Gludovatz, J. Watts, A.P. Tomsia, G.E. Hilmas, R.O. Ritchie, A novel approach to developing biomimetic ("nacre-like") metal-compliant-phase (nickel–alumina) ceramics through coextrusion, *Adv. Mater*. 28 (2016) 10061-10067.

[80] M.E. Launey, R.O. Ritchie, On the fracture toughness of advanced materials, *Adv. Mater*. 21 (2009) 2103-2110.

[81] Z. Chen, J.J. Mecholsky, Control of strength and toughness of ceramic/metal laminates using interface design, *J. Mater. Res*. 8 (1993) 2362-2369.

[82] R.G. Munro, Evaluated material properties for sintered α-alumina, *J. Am. Ceram. Soc.* 8 (1997) 1919-1928.

[83] W.D. Jenkins, T.G. Digges, Effect of temperature on the tensile properties of high-purity nickel, *J. Res. Nat. Bur. Stand.* 48 (1952) 313-321.